NTNU

Norwegian University of
Science and Technology

Simulation of floating bodies in waves using REEF3D

Jiayi Zheng Lu

Civil and Environmental Engineering
Submission date: June 2017
Supervisor: Hans Sebastian Bihs, IBM
Co-supervisor: Arun Kamath, IBM

Norwegian University of Science and Technology
Department of Civil and Environmental Engineering

NORWEGIAN UNIVERSITY OF SCIENCE AND TECHNOLOGY
DEPARTMENT OF CIVIL AND TRANSPORT ENGINEERING

Report Title:	Date: 28/06/2017			
Simulation of floating bodies in waves using REEF3D	Number of pages (incl. appendices): 76			
	Master Thesis	X	Project Work	

Name:
Jiayi Zheng Lu

Professor in charge/supervisor:
Hans Bihs

Other external professional contacts/supervisors:
Arun Kamath

Abstract:
The aim of this thesis is the validation of the 6 degrees of freedom (DOF) algorithm implemented in REEF3D for floating bodies. The 6DOF of a free-floating structure are three displacements in each axis and three rotations around each axis.
REEF3D is an open source Computational Fluid Dynamics (CFD) code developed in the Department of Civil and Environmental Engineering at NTNU. In the thesis, the numerical model used for the development of the simulations is explained as well as the main features and options of the software. Reynolds-Averaged Navier-Stokes (RANS) equations in three dimensions govern the numerical model. A fifth order WENO scheme is used to discretize the convection term in the RANS equations. Chorin's Projection Method is used to obtain the pressure term in the RANS equations. The Bi-Conjugate Gradient Stabilized method is used to solve the Poisson equation from the pressure model. The turbulence model adopted for the fluid is *k-w*. Second-order and third-order Total Variation Diminishing Runge-Kutta schemes are used for time treatment for momentums and the free surface, respectively. The numerical grid used is a Cartesian staggered grid with the ghost cell immersed boundary method. Simulations are carried out in a Numerical Wave Tank (NWT) composed of a wave generation zone, the wave tank and a numerical beach zone. The wave generation and numerical beach zones are explained in the numerical model. The turbulence near the solid boundaries or walls of the NWT is also considered with the wall law and no-slip condition for velocities. Wave theories used are Airy linear and second-order Stokes. The free surface is obtained with the level set method. The 6DOF algorithm used to obtain the forces, momentums and motions of the floating body is explained in detail.
Two cases are compared with experimental data found in the literature. Another case is performed as further study. The first case is a two-dimensional simulation on a free-floating rectangular barge in non-linear waves using the second-order Stokes wave theory. The DOF are heave, pitch and surge. The motions are compared with experimental data. The undisturbed wave elevation is also compared. Different grid sizes are used to determine the differences between each grid result, stability and convergence to experimental results.
The second case is a three-dimensional simulation of the same floating body with the same wave conditions. Here, the effects of wall distance on the floating body motions is studied. Three tank widths with the same barge breadth are set to discern the effects of the gap between the floating body and the wall tank on the body motions. Results of motions and wave elevation are compared with the two-dimensional simulation and between the three-dimensional cases.
The validation case for three dimensions consists on a free-floating ship in linear waves. The ship is DTMB5512 which is a geosim of a US Navy's surface combatant. The ship geometry is imported with a function of REEF3D from a STL file. The DOF for the comparison with experimental data are heave and pitch. The undisturbed wave elevation is compared. The level set method definition of the geometry of the ship is discussed with different grid sizes. This analysis defines the choice of the grid size. Results of validation cases for two and three dimensions show favourable good agreement with experimental data.

Keywords:

1. Floating bodies
2. 6DOF
3. Fluid-structure interaction
4. REEF3D

_____

THIS PAGE INTENTIONALLY LEFT BLANK.

Acknowledgements

As an exchange student, writing a thesis abroad present difficulties, not only for the language. The adaptation to a new environment, culture and work practices is always challenging.

That's why without the guidance of my supervisor, Hans, and my co-supervisor, Arun, this thesis could not have been possible. Not only this thesis but the complete REEF3D software is possible thanks to them, and the REEF3D team. I want to thank Hans for his help, patience and possibilities he gave me which are uncommon in my home university like attending and speaking in conferences or co-authoring a paper. Special thanks to Arun for his enormous assistance, his always predisposition for helping and his availability to answer my questions. Also, thanks the REEF3D team which I met in the conference. You are all aboard on an amazing project which is giving excellent results.

I could not forget my home university for setting the foundations of my knowledge. Also my family, especially my mother who is always supporting me with her incredible efforts. My friends, old ones back at home and new ones in Trondheim. Without them, this thesis would have not been possible.

THIS PAGE INTENTIONALLY LEFT BLANK.

CONTENTS

LIST OF TABLES

THIS PAGE INTENTIONALLY LEFT BLANK.

LIST OF FIGURES

NOMENCLATURE

Symbols

Δt	Time-step size
ϵ	Thickness of interface
κ	Von Kármán constant
λ	Wavelength
$\mathbf{r_{cg}}$	Distance of the centre of gravity from the origin of the body grid
$\mathbf{r}$	Distance from a surface cell to the origin of the body-fitted coordinate system
$\mathbf{S}$	Rate of strain
μ	Dynamic viscosity
ν	Kinematic viscosity
ν_t	Eddy viscosity
Ω	Floating body surface
ω	Specific turbulent dissipation
$\overline{u_i u_j}$	Reynold stresses
ϕ	Level Set Function
ϕ, θ, ψ	Euler angles
ρ	Density
$\tilde{\epsilon}$	Regularization parameter
a	Wave amplitude

c	cos
D	Diffusion term
d	Water depth
g	Gravity
H	Wave height
h	Heigth
I_i	Moment of inertia in i direction
IS	Smoothness indicator
k	Turbulent kinetic energy in section 2.3: Turbulence model and subsection 2.7.1: Boundary treatment
k	Wave number
K, M, N	Momentums in x, y, z direction
k_s	Equivalent sand roughness
l	Length
$L_{i,e}$	Moment in i direction
m	Mass of the body
p	Pressure
p, q, r	Angular velocities in x, y, z direction
P_k	Turbulent production rate
S	Source term
s	sin
$S(\phi)$	Smooth signed function
T	Wave period
t	tan in section 2.9: 6 DOF algorithm
t	Time
u, v, w	Linear velocities in x, y, z direction
u^+	Dimensionless wall velocity
u_i	Velocity in i direction
u_i^*	Intermediate velocity
w	Observed wave angular frequency
X, Y, Z	Forces in x, y, z direction

x_i	Cartesian coordinates
x_{cg}, y_{cg}, z_{cg}	Position vector
dx	Grid size

Abbreviations

BiCGSTAB	Bi-Conjugate Gradient Stabilized
CFD	Computational Fluid Dynamics
CFL	Courant Friedrichs Lewy
DOF	Degree Of Freedom
DTMB	David Taylor Model Basin
EFD	Experimental Fluid Dynamics
ENO	Essentially Non-Oscillatory
FSI	Fluid Structure Interaction
LCG	Longitudinal Centre of Gravity
MPI	Message Passing Interface
NS	Navier-Stokes
NTNU	Norges teknisk-naturvitenskapelige universitet
NWT	Numerical Wave Tank
PJM	Projection Method
RANS	Reynolds-Averaged Navier-Stokes
TVD	Total Variation Diminishing
URANS	Unsteady Reynold-Averaged Navier-Stokes
VCG	Vertical Centre of Gravity
WENO	Weighted Essentially Non-Oscillatory

THIS PAGE INTENTIONALLY LEFT BLANK.

CHAPTER 1

INTRODUCTION

Fluid-structure interaction (FSI) is an extensively studied field in engineering. There are floating and moored structures in marine engineering like wave energy conversion devices, oil platforms or wind turbines. In civil engineering, nearby the coast, there are also floating structures like piers or breakwaters. Breakwaters are needed for coast and harbour defence against the action of the sea. In the last years, the development of the analysis and technology has improved significantly, allowing an increase of the size of the structures. For example, from simple piers to large floating cruise terminals in the harbour of Oslo. Floating structures can also be a solution for the overpopulation and cost of housing in crowded cities with rivers by building floating houses like in IJburd (Amsterdam). Besides, floating structures are a solution for energy consumption with renewable energy. A present example is a floating solar farm in China. The Dogger island project in the North Sea with solar panels and wind turbines is a future example under study. The climate change is also creating a need for new solutions to control the increase of sea water level and wave height during storms. Here, floating breakwaters are a viable option compared to the traditional procedures, especially, for areas with a great water depth. For the design of the structures, new models or tools that are able to calculate displacements, motions and forces on the structure with a higher accuracy are needed.

Floating structures have 6 degrees of freedom (DOF) which are three displacements and three rotations, shown in Fig. 1.1. Displacements are surge, sway and heave in x, y and z direction, respectively. Rotations are roll, pitch and yaw around x, y and z axis, respectively.

Analytical methods were used to resolve these problems in the past but they don't take into account parameters like fluid viscosity or non-linear effects. Thus, these are limited tools to solve problems of this kind of nature. Since the last decades, numerical simulation with Computational Fluid Dynamics (CFD) software is flourishing. Floating structures present several challenges caused by the non-linearity of the free surface and the complexity of

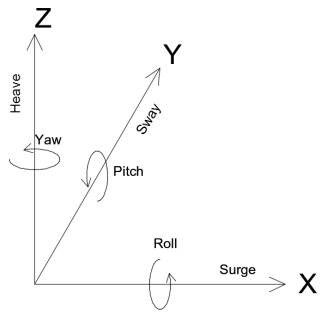

Figure 1.1: 6 degrees of freedom. Displacements and rotations.

the problems to solve like turbulence, wave breaking or motion of the body. Navier-Stokes (NS) or Reynolds-Averaged Navier-Stokes equations (RANS) are used by several models using the finite difference method or the finite volume method with techniques like level set method and volume of fluid to obtain the free surface. The free surface can be computed as a single-flow, Tanaka and Kashiyama (2006), neglecting the effect of the air or a two-phase flow including the effect of it, Bihs et al. (2016). First studies used a single-phase flow with the arbitrary lagrangian-eulerian method, Takashi (1994), where the mesh moves with the boundary and interface, all the time. However, this method is not satisfactory for problems where the free surface is not smooth and continuous or has large deformations. Another approach on the arbitrary lagrangian-eulerian method is the immersed boundary, introduced by Peskin (2002). On a fixed Cartesian mesh, the flow equations are solved and the effect of the boundary is computed with an imaginary force field. With the level set function, the interface between water and air, in the case, becomes the zero-contour of the level set function. The level set immersed boundary method has been used to study complex geometries, in Calderer et al. (2014) and Yang and Stern (2009).

1.1 Objectives

The objective of this thesis is the validation of the 6DOF algorithm with different cases or applications. The first case is a two-dimensional simulation of a floating body in waves. The body is a rectangular barge. The motions of the floating body with different grid sizes will be compared with experimental data. Motions for the comparison are heave, pitch and surge. The undisturbed wave elevation is also compared. A simulation with a different wavelength will also be performed. With this case, numerical results in two dimensions with the 6DOF algorithm and experiment results are compared.

The second case is a three-dimensional case of a floating body in waves. The case is the three-dimensional application of the first case. The laboratory experiments to obtain the experimental data in the first case are performed trying to simulate two-dimensional conditions. In the experiment, some DOF are restrained to achieve two-dimensional conditions

minimizing the effect of the distance with the flume wall. With this case, the effect of wall distance on the floating body and its motion is studied. Three different wall distances will be simulated with the same body breadth and wave conditions as the first case.

The third case is a three-dimensional ship simulation. The ship is a DTMB 5512 model which is a geosim of a U.S. Navy's ship design for a surface combatant with a sonar dome bow and transom stern. The ship is under the effect of waves only. The motions of the ship are heave and pitch. The motions and wave elevation will be compared with experimental data.

All the cases are simulated with REEF3D, an open source CFD code in development at the Department of Civil and Environmental Engineering at Norwegian University of Science and Technology (NTNU), Norway. The software has been used in several applications being validated for wave forces and free surface analysis around horizontal cylinders in tandem by Ong et al. (2017) or waves forces and wave elevation around vertical cylinders by Kamath et al. (2015), among others. The order of the thesis is: firstly, the methodology is explained including governing equations of the model, turbulence model, pressure treatment, free surface treatment, numerical grid, numerical wave tank, 6DOF algorithm and parallelization. Secondly, the cases are explained with the configuration of the simulation and the experiment for the validations. Numerical results for each case will be discussed. Lastly, conclusions and outlook of the document.

THIS PAGE INTENTIONALLY LEFT BLANK.

CHAPTER 2
NUMERICAL MODEL

In this chapter, the numerical model used for the development of this thesis will be explained. The software used is REEF3D which has several options for turbulence modelling, time treatment schemes, convection-discretization or pressure solvers among others. However, only the most important features and the options that are used in the thesis are explained in this chapter. For more information about all the options available in the software, consult the REEF3D team and the user guide.

2.1 Governing equations

Navier-Stokes equations in three dimensions are the governing equations of the numerical model. Mass conservation and linear momentum conservation are the base of NS equations. The density of the fluid remains constant so the fluid, water in the thesis, is assumed to be incompressible. The conservation of mass is given by the continuity equation:

$$\frac{\partial u_i}{\partial x_i} = 0 \tag{2.1}$$

Conservation of linear momentum leads to NS equation (Versteeg and Malalasekera, 2007):

$$\frac{\partial u_i}{\partial t} + \frac{\partial u_i u_j}{\partial x_j} = \frac{\partial}{\partial x_j}\left(\mu \frac{\partial u_i}{\partial x_j}\right) - \frac{1}{\rho}\frac{\partial p}{\partial x_i} \tag{2.2}$$

With Eq. (2.1) and (2.2) together, the Navier-Stokes equation can be rewritten as the RANS equation:

$$\frac{\partial u_i}{\partial t} + u_j \frac{\partial u_i}{\partial x_j} = -\frac{1}{\rho}\frac{\partial p}{\partial x_i} + \frac{\partial}{\partial x_j}\left[\nu\left(\frac{\partial u_i}{\partial x_j} + \frac{\partial u_j}{\partial x_i}\right) - \overline{u_i u_j}\right] + g_i \tag{2.3}$$

where u is the velocity over time t, x is the spatial geometrical scale, ρ is the fluid density, $\nu = \frac{\mu}{\rho}$ is kinematic viscosity with μ dynamic viscosity, p is pressure, $\overline{u_i u_j}$ represents the Reynold stresses and g is gravity.

In Eq. (2.3), the left side represents the inertial forces composed by a transient term in form of a variation of velocity over time and a convection term. On the right side, the first term represents the pressure forces also known as volumetric stress tensor. The second term represents the viscous forces with a diffusive term with second derivatives respect to the coordinates involved. The last term represents the external forces applied to the fluid.

2.1.1 Numerical approach

In order to solve NS equations, partial derivatives are replaced by a finite difference approximation. As a result, a new algebraic equation or system of algebraic equations is obtained which are an approximate solution to the original equation in partial derivatives. There are three main numerical approaches: finite volume method, finite difference method and finite element method.
Finite volume method is the main discretization method used in CFD software nowadays. In this approach, the domain is divided in cells or control volumes. In these cells, the formulation of the integrated partial differential equations results in a balance equation. Then, the balance equations are approximated by numerical integration. The function values and derivatives are approximated by interpolation with nodal values. The solution of the discrete algebraic system is assembled. The finite volume method distinguishes from other methods for the conservation of the properties in each cell such as mass, momentum and energy.
The approach used in REEF3D is the finite difference method. For this method, the domain is divided in points forming a grid. A linear combination of function values at grid points is used as an approximation for the partial differential equation.

When a partial difference equation is substituted with a finite difference approximation, errors are introduced in each step, for example, truncation errors. These methods use every step a smaller interval which is expected to converge to the exact solution with the accuracy required. Thus, the following properties should be fulfil:

- Consistency: a finite difference method is consistent if it reduces the difference between the original differential equation and the numerical approximation as the increment reduces.

- Stability: a finite difference approximation is stable if the errors or perturbations in the numerical solution remains restrained or decay as it progress through the steps.

- Convergency: if the two requirements above are accomplished, the numerical approximation is convergent expressed by Lax theorem (Lax and Richtmyer, 1956): “for the numerical solution of partial differential equations, for a *consistent* finite difference method for a well-posed linear initial value problem, the method is *convergent* if and only if it is *stable*". In other words, a finite difference method is

convergent if it approaches to the true solution of the partial differential equation as the increments go to zero.

2.2 Convection discretization

In Eq. (2.3) the convective term needs to be discretized before solving the equation. REEF3D has different implementations to resolve convection-discretization using the finite difference method. The accuracy depends on the points or stencil generated for the evaluation with the finite difference method. There are several schemes implemented in the code:

- First-Order Upwind (FOU) scheme introduced by Courant et al. (1952). This scheme evaluate the property on the cell with the values upstream and then compute the value at the centre of the cell. The first-order uses a point upstream the flow. It is given by:

$$\frac{\partial \Phi}{\partial x_j} = \frac{\Phi_i - \Phi_{i-1}}{\Delta x_j} \tag{2.4}$$

- Central difference scheme (CDS) of second and fourth order. Central difference scheme, on the contrary to first-order upwind scheme, uses two points. A point upstream and another downstream to calculate the cell, which is the centre. The second order central difference scheme is:

$$\frac{\partial \Phi}{\partial x} = \frac{\Phi_{i+1} - \Phi_{i-1}}{2\Delta x} \tag{2.5}$$

  The fourth order central difference scheme with four points, two upstream and two downstream the cell, is given by:

$$\frac{\partial \Phi}{\partial x} = \frac{-\Phi_{i+2} + 8\Phi_{i+1} - 8\Phi_{i-1} + \Phi_{i-2}}{12\Delta x} \tag{2.6}$$

- Sharp and Monotonic Algorithm for Realistic Transport (SMART) scheme developed by Gaskell and Lau (1988) uses a curvature-compensated convective transport approximation and a piecewise linear normalized variable formulation.

- Quadratic Upwind Interpolation of Convective Kinetics (QUICK) scheme presented by Leonard (1975), is a high-order scheme that considers three points upstream through a quadratic interpolation to approximate the function value in the cell. Depending on the sign of the flux incoming to the cell, the scheme takes two points upstream or two points downstream creating a parabola shape with these points upstream or downstream.

- Weighted Essentially Non-Oscillatory (WENO) scheme introduced by Jiang and Shu (1996). This scheme is used in this thesis with a fifth-order WENO. WENO scheme is capable of achieving high accuracy in complex smooth regions or with strong discontinuities. These stencils are weighted depending on their smoothness, with the smoothest stencil contributing the most significantly. The scheme is implemented in a conservative framework for the convection discretization of flow velocities.

$$u_i \frac{\partial u_i}{\partial x_i} \approx \frac{1}{\Delta x}(\tilde{u}_{i+1/2}\, u_{i+1/2} - \tilde{u}_{i-1/2}\, u_{i-1/2}) \tag{2.7}$$

The convection velocity $\tilde{u}$ is obtained at the cell faces through simple interpolation. For the cell face with subscript $i + 1/2, u_{i+1/2}$ is reconstructed with the WENO scheme based on the weighted sum of three Essentially Non-Oscillatory (ENO) stencils:

$$U^{\pm}_{i+1/2} = w_1^{\pm}\, U^{1\pm}_{i+1/2} + w_2^{\pm}\, U^{2\pm}_{i+1/2} + w_3^{\pm}\, U^{3\pm}_{i+1/2} \tag{2.8}$$

The $\pm$ sign indicates the upstream direction. U^1, U^2 and U^3 represent the three possible ENO stencils. For upstream direction in the positive i-direction:

$$\begin{aligned} U^{1\pm}_{i+1/2} &= \frac{1}{3}u_{i-2} - \frac{7}{6}u_{i-1} + \frac{11}{6}u_i \\ U^{2\pm}_{i+1/2} &= -\frac{1}{6}u_{i-1} + \frac{5}{6}u_i + \frac{1}{3}u_{i+1} \\ U^{3\pm}_{i+1/2} &= -\frac{1}{3}u_i + \frac{5}{6}u_{i+1} - \frac{1}{6}u_{i+2} \end{aligned} \tag{2.9}$$

The choice of the non-linear weights $w_n^{\pm}$ relies on the smoothness indicators IS which measures the smoothness of the function in the stencil. The ENO stencil with the smoothest solution will be assigned the largest weight. For stencils with larger gradients, the weights will be smaller.

$$w_1^{\pm} = \frac{\alpha_1^{\pm}}{\alpha_1^{\pm} + \alpha_2^{\pm} + \alpha_3^{\pm}},\ w_2^{\pm} = \frac{\alpha_2^{\pm}}{\alpha_1^{\pm} + \alpha_2^{\pm} + \alpha_3^{\pm}},\ w_3^{\pm} = \frac{\alpha_3^{\pm}}{\alpha_1^{\pm} + \alpha_2^{\pm} + \alpha_3^{\pm}} \tag{2.10}$$

and

$$\alpha_1^{\pm} = \frac{1}{10}\frac{1}{(\tilde{\epsilon} + IS_1^{\pm})^2},\ \alpha_2^{\pm} = \frac{6}{10}\frac{1}{(\tilde{\epsilon} + IS_2^{\pm})^2},\ \alpha_1^{\pm} = \frac{3}{10}\frac{1}{(\tilde{\epsilon} + IS_3^{\pm})^2} \tag{2.11}$$

with the regularization parameter $\tilde{\epsilon} = 10^{-6}$ to avoid the denominator to become zero and the following smoothness indicators:

$$
\begin{aligned}
IS_1^{\pm} &= \frac{13}{12}(q_1 - 2q_2 + q_3)^2 + \frac{1}{4}(q_1 - 4q_2 + 3q_3)^2 \\
IS_2^{\pm} &= \frac{13}{12}(q_2 - 2q_3 + q_4)^2 + \frac{1}{4}(q_2 - q_4)^2 \\
IS_3^{\pm} &= \frac{13}{12}(q_3 - 2q_4 + q_5)^2 + \frac{1}{4}(3q_3 - 4q_4 + q_5)^2
\end{aligned}
\tag{2.12}
$$

2.3 Turbulence model

Turbulence modelling is important in marine civil engineering or hydraulics applications for the energy dissipation in the process. In marine civil engineering, floating structures that are still or moving in waves will produce turbulence and vortices around themselves. Besides, stresses are produced on the structure.
In order to resolve the turbulence phenomena there are different methods. The most accurate is the direct numerical simulation (DNS), the NS equation is directly solved numerically, capturing all the scales present from the smallest to the largest eddies. However, DNS is computationally expensive for memory, processing, and storage cost. Large Eddy Simulation (LES) proposed by Smagorinsky (1963), is another approach to solve the turbulence model. In this method, the large eddies are computed directly and the small scale eddies are modelled with a numerical model, reducing the computational cost. For the applications in engineering, the scales are usually large so a LES or DNS approach are not possible in terms of computational cost. Either LES or DNS are difficult to use for complex geometries, being possible with small scales and simple geometries or low Reynolds numbers (Zhiyin, 2015).
Another approach is RANS method in which only the averaged quantities are solved. Instantaneous turbulent motion from all scales is obtained through a turbulence model. The computational cost is less in comparison to DNS or LES methods and is applicable to large scale simulations. REEF3D has several models implemented in the code: k-ϵ (Launder and Spalding, 1974), Explicit Algebraic Reynolds Stress Models (EARSM) (Wallin and Johansson, 2000), Unsteady Reynold-Averaged Navier-Stokes (URANS), LES and k-ω model (Wilcox, 1995). The numerical turbulence model used in this document is the last mentioned, k-ω model.

2.3.1 *k*-ω model

In Eq. (2.3), the Reynolds stress term is replaced with the Boussinesq-approximation (Boussinesq, 1877):

$$
-\overline{u_i u_j} = \nu_t \left(\frac{\partial u_i}{\partial x_j} + \frac{\partial u_j}{\partial x_i} \right) - \frac{2}{3} k \delta_{ij} \tag{2.13}
$$

obtaining a new RANS equation:

$$\frac{\partial u_i}{\partial t} + u_j \frac{\partial u_i}{\partial x_j} = -\frac{1}{\rho}\frac{\partial p}{\partial x_i} + \frac{\partial}{\partial x_j}\left[(\nu + \nu_t)\left(\frac{\partial u_i}{\partial x_j} + \frac{\partial u_j}{\partial x_i}\right) - \frac{2}{3}k\delta_{ij}\right] + g_i \tag{2.14}$$

where the eddy viscosity ν_t in the Eq. (2.14) is obtained with the following equation:

$$\nu_t = c_\mu \frac{k}{\omega} \tag{2.15}$$

To obtain the eddy viscosity ν_t and the Reynolds stress term, the turbulent kinetic energy k and the specific turbulent dissipation ω solutions are found by solving the following equations:

$$\frac{\partial k}{\partial t} + u_j \frac{\partial k}{\partial x_j} = \frac{\partial}{\partial x_j}\left[\left(\nu + \frac{\nu_t}{\sigma_k}\right)\frac{\partial k}{\partial x_j}\right] + P_k - \beta_k k\omega \tag{2.16}$$

$$\frac{\partial \omega}{\partial t} + u_j \frac{\partial \omega}{\partial x_j} = \frac{\partial}{\partial x_j}\left[\left(\nu + \frac{\nu_t}{\sigma_\omega}\right)\frac{\partial \omega}{\partial x_j}\right] + \frac{\omega}{k}\alpha P_k - \beta\omega^2 \tag{2.17}$$

where P_k is the turbulent production rate, the coefficients have the value $\alpha = \frac{5}{9}$, $\beta_k = \frac{9}{100}$, $\beta = \frac{3}{40}$, $\sigma_k = 2$ and $\sigma_w = 2$.

In the oscillatory wave motion the rate of strain can be large. The boundary layer is not resolved explicitly in the model but is accounted for with the wall laws in the turbulence model explained in subsection 2.7.1. To avoid the overproduction of turbulence in highly strained flow outside the boundary layer, a constraint is implemented for the eddy viscosity, after Durbin (2009):

$$\nu_t = min\left(\frac{k}{\omega}, \sqrt{\frac{2}{3}}\frac{k}{|\mathbf{S}|}\right) \tag{2.18}$$

The rate of strain $\mathbf{S}$ can give inaccurate results near the boundary between air and water so an additional turbulent damping is added. The specific turbulent dissipation at the free surface is given in Naot and Rodi (1982):

$$\omega_s = \frac{c_\mu^{-\frac{1}{4}}}{\kappa} k^{\frac{1}{2}} \cdot \left(\frac{1}{y'} + \frac{1}{y^*}\right) \tag{2.19}$$

where $c_\mu = 0.07$ and $\kappa = 0.4$. The virtual origin of the turbulent length scale y' was empirically found to be 0.07 times the mean water depth (Hossain and Rodi, 1980). Including the distance y^* from the nearest wall gives a smooth transition from the free surface value

to the wall boundary value ω. The term for the specific turbulent dissipation ω_s is activated around the interface of thickness ϵ by multiplying it with the Dirac delta function $\delta(\phi)$:

$$\delta(\phi) \begin{cases} \frac{1}{2\epsilon}\left(1+\cos(\frac{\pi\phi}{\epsilon})\right) & if\ |\phi| < \epsilon \\ 0 & else \end{cases} \tag{2.20}$$

2.4 Pressure treatment

In Eq. (2.3), the pressure can't be obtained directly as velocity and pressure are coupled in incompressible fluids. Besides, the non-linear terms render the procedure high computational. The continuity equation is taken into account to obtain a solution. REEF3D offers different solvers for the pressure: Pressure implicit with split operator (PISO), Semi Implicit Method for Pressure Linked Equation (SIMPLE) and Projection Method (PJM).

- Semi Implicit Method for Pressure Linked Equation (SIMPLE) was developed by Patankar and Spalding (1972), is an iterative algorithm that introduces the pressure into the continuity equation. SIMPLE solves the pressure equation under-relaxation and corrects the velocities with the pressure field obtained. This process is repeated until convergence is achieved.

- Pressure implicit with split operator (PISO) was proposed by Issa (1986) as an extension of SIMPLE algorithm without iterations, with large time-steps and a lesser computing effort. The algorithm splits the operators. First, predicting a value using an implicit predictor and correcting it after, with multiple explicit corrector steps. Each time-step certain variables are predicted and corrected, for example, velocity.

- PJM is the most used of the three methods presented. Chorin's PJM (Chorin, 1968) is adopted in this thesis which separates the velocity and pressure fields. The momentum equation is computed with an intermediate velocity u_i^* ignoring the pressure term:

$$\frac{\partial u_i^*}{\partial t} + u_j^n \frac{\partial u_i^n}{\partial x_j} = \frac{\partial}{\partial x_j}\left[(\nu+\nu_t)\left(\frac{\partial u_i^n}{\partial x_j} + \frac{\partial u_j^n}{\partial x_i}\right)\right] + g_i \tag{2.21}$$

  Then, the projection step is taken, where the intermediate velocity u_i^* is corrected to obtain the solution of the time-step u_i^{n+1} with the pressure term added:

$$\frac{\partial(u_i^{n+1} - u_i^*)}{\partial t} = -\frac{1}{\rho(\phi^n)}\frac{\partial p^{n+1}}{\partial x_i} \tag{2.22}$$

  To compute the right-hand side of Eq. (2.22), the pressure term p at time-step $n+1$ should be known. To obtain this, the divergence of velocity u_i^{n+1} should be zero

following the continuity equation where the divergence is zero for an incompressible fluid. This results in a Poisson equation:

$$\frac{\partial}{\partial x_i}\left(\frac{1}{\rho(\phi^n)}\frac{\partial p^{n+1}}{\partial x_i}\right) = \frac{1}{\Delta t}\frac{\partial u_i^*}{\partial x_i} \tag{2.23}$$

2.4.1 Iterative solver

Poisson equation (2.23) can be solved with direct methods, iterations and multi-grid methods. REEF3D has implemented iterative and multi-grid solvers with pre-conditioners. Thanks to the High Performance Pre-conditioners (HYPRE) implementation, the code has access to a library for the solution of large, sparse linear systems on parallel computers. Among all of the systems implemented, some are explained next:

- PFMG introduced by Ashby and Falgout (1996) is a semi-coarsening multi-grid method for solving scalar diffusion equations on rectangular grids discretized with up to 9-point stencils in 2D and up to 27-point stencils in 3D.

- SMG introduced by Stone (1968) is also a semi-coarsening multi-grid method for solving scalar diffusion on rectangular grids. It is more robust than PFMG, especially for anisotropies that vary in either strength or direction across the domain but it is also more expensive per iteration for this reason.

- AMG (BoomerAMG) is an unstructured Algebraic Multi-Grid (AMG) developed by Henson and Yang (2002). AMG has the advantage that it does not require an explicit grid geometry increasing the type of problems that can be solved with the system. However, this advantage makes it a complex and difficult algorithm to achieve a good convergence, low memory and computational requirements.

- Bi-Conjugate Gradient Stabilized (BiCGSTAB) is the method used in this thesis. It is based on the conjugate gradient, an iterative algorithm to obtain the solution of particular systems of linear equations. It was developed by Hestenes and Stiefel (1952). The conjugate gradient method begins with a guess for the solution and iterates, improving step by step. The method can be used only for real symmetric positive definite linear systems. Later, the Bi-Conjugate gradient was developed by Fletcher (1976) that unlike the conjugate gradient method does not require a symmetric or orthogonal linear system. The Bi-Conjugate gradient algorithm solves not only the original system but also the system with the orthogonal matrix requiring more computing power and memory storage. The BiCGSTAB was developed by van der Vorst (1992) being a variant of Bi-Conjugate gradient with a faster and smoother convergence. The method can be preconditioned $\mathbf{K} = \mathbf{K_1}\mathbf{K_2} \approx \mathbf{A}$ to accelerate the convergence computing $\mathbf{K}$ as a middle step before calculating $\mathbf{A}$.

2.5 Time treatment

For time domain, REEF3D has different schemes: Adams-Bashforth, second, third and fourth-order Total Variation Diminishing (TVD) Runge-Kutta. The schemes used in the document are second-order TVD Runge-Kutta for momentum equations and third-order TVD Runge Kutta for the free surface using level set method. The higher order requires more computational power but it results in a better accuracy and stability. A numerical method is TVD if the total variation for every step is smaller than the previous step so a TVD scheme maintains the monotonicity.
The second-order TVD Runge-Kutta time scheme for a generic variable Φ, after Shu, C. W. and Osher (1988):

$$\begin{aligned} \Phi^{(1)} &= \Phi^n + \Delta t L(\Phi^n) \\ \Phi^{n+1} &= \frac{1}{2}\Phi^n + \frac{1}{2}\Phi^{(1)} + \frac{1}{2}\Delta t L(\Phi^{(1)}) \end{aligned} \tag{2.24}$$

The equations of the third-order Runge-Kutta scheme for the generic variable Φ as given in Shu, C. W. and Osher (1988):

$$\begin{aligned} \Phi^{(1)} &= \Phi^n + \Delta t L(\Phi^n) \\ \Phi^{(2)} &= \frac{3}{4}\Phi^n + \frac{1}{4}\Phi^{(1)} + \frac{1}{4}\Delta t L\left(\Phi^{(1)}\right) \\ \Phi^{n+1} &= \frac{1}{3}\Phi^n + \frac{2}{3}\Phi^{(2)} + \frac{2}{3}\Delta t L\left(\Phi^{(2)}\right) \end{aligned} \tag{2.25}$$

To maintain the stability of the simulation, the fluid should not progress more than one cell per time-step. This is called the Courant-Friedrichs-Lewy (CFL) condition (Courant et al., 1967). In one dimension, the CFL would be:

$$C = \frac{u\Delta t}{\Delta x} \leq C_{max} \tag{2.26}$$

where the number C is called the Courant number and it is dimensionless, u is the magnitude of velocity, Δt is the time-step and Δx is the length interval. The value of C_{max} is usually 1. The schemes above present good numerical stability for CFL numbers below 1 (Shu, C. W. and Osher, 1988). To control the CFL number inside the limit, adaptive time-stepping is used. It takes the influence from velocity u, diffusion D and the source term S. The time-step size Δt is determined as follows:

$$\Delta t \leq 2\left(\left(\frac{|u|_{max}}{dx} + D\right) + \sqrt{\left(\frac{|u|_{max}}{dx} + D\right)^2 + \frac{4|S_{max}|}{dx}}\right)^{-1} \tag{2.27}$$

with the contribution from the diffusion term D:

$$D = max(\nu + \nu_t) \cdot \left(\frac{2}{(dx)^2} + \frac{2}{(dy)^2} + \frac{2}{(dz)^2} \right) \tag{2.28}$$

2.6 Numerical grid

A Cartesian grid is used as the numerical grid for the simplicity defining geometries with coordinates or implementing algorithms for the numerical model. The grid used is staggered. The scalar variables like pressure, are stored in the cell centres of the control volume and the velocity or momentum are located at the cell faces. The staggered Cartesian grid approach may be inflexible for the complex geometries that the fluid may take, near solid boundaries. The fluid may have large deformations or steep changes in a small distance which suppose a problem to represent in a Cartesian grid. In addition, floating bodies may present sharp edges and irregular shapes which suppose a problem to generate a high quality grid. An approach is to use an immersed boundary, where the boundary intersects with an underlying Cartesian grid. With this technique, a new boundary is formed with the grid cells cut by the immersed boundary. The use of ghost cells with an immersed boundary method was introduced by Berthelsen and Faltinsen (2008) as an alternative. The ghost cells are fictitious cells inside the boundary or solid and they are updated by extrapolating values from the flow field and the boundary. The ghost cell immersed boundary method is used in this document.

2.7 Numerical Wave Tank

The simulation with waves are performed in a numerical wave tank (NWT). This is an analogue equivalent to a physical laboratory wave flume. With the increase in computation power and CFD advances, a NWT is a plausible option for experiments. For a validated CFD code, the advantages of a NWT are obvious in time and cost. It requires less time to set up a simulation than a laboratory experiment, as well as, the cost to obtain the results. The spatial domain is discretized with a Cartesian grid for the easiness when defining the geometry. The spatial domain in the NWT is divided in three zones: the wave generation zone, the wave tank and the numerical beach zone. The wave generation zone is one wavelength long and the numerical beach zone is two wavelengths long.

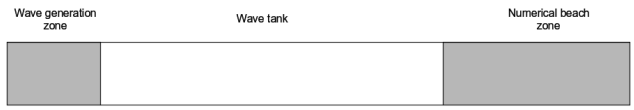

Figure 2.1: Zones in the numerical wave tank.

2.7.1 Boundary treatment

The boundaries in the NWT can be treated as inflow, outflow, solid boundaries, wave generation, numerical or active beach. For the inflow and outflow input, it can be a constant value or hydrograph either for inflow, outflow or both. Wave generation and wave absorption is explained in sub-section 2.7.2. In case of the solid boundary, it is materialised as a wall. The boundary can be either slip or no-slip for velocities. No-slip condition assumes that the fluid near the the boundary will have zero velocity relative to it. No-slip condition is used in this document. A roughness value and wall law, rough or smooth, should also be adopted as an input. The wall roughness is calculated using Schlichting's formula (Schlichting, 1979):

$$u^+ = \frac{1}{\kappa} \ln \left(\frac{30d}{k_s} \right) \tag{2.29}$$

where u^+ is the dimensionless wall velocity, κ is the von Kármán constant which was found to be 0.4 from experiments, d the water depth and k_s the equivalent sand roughness. This parameter is the input value in REEF3D to define the roughness of the wall. Near the walls in the NWT, the turbulent production is equal to the dissipation of k. The wall function for the specific turbulent dissipation ω for a bed cell with the distance Δy_p from the wall to the centre of the cell is then:

$$\epsilon_{wall} = -\frac{c_\mu^{3/4} k_w^{1/2} U_w^+}{\Delta y_p} \tag{2.30}$$

The formula gives the value for turbulent dissipation ϵ directly. The turbulent kinetic energy k at the wall is treated by integrating the source terms of Eq. (2.16) over the bed cell:

$$\int (P_k - \epsilon_{wall})\rho = \left[\frac{\tau_w u_w}{\Delta y_p} - \frac{c_\mu^{3/4} k_w^{1/2} U_w^+}{\Delta y_p} \right] \tag{2.31}$$

The rough wall law is then used to determine the wall shear stress τ_w and the dimensionless u^+. The terms in Eq. (2.31) are discretized as source terms in the transport equation for k.

2.7.2 Wave generation and absorption

In the NWT there are three zones. In the first zone, the waves are generated. The second zone is the wave tank. In the last zone, the waves are dissipated with a numerical beach or the flow discharged with an outflow. For the wave generation zone, REEF3D has Dirichlet type or relaxation methods.
Dirichlet generation or dissipation follows the Dirichlet boundary condition for a known function defined in the boundary. The method does not generate the highest quality waves due to the motion of the free surface and the flow direction changes.

The relaxation method can be used for the generation and dissipation of waves in the wave generation zone and numerical beach (Larsen and Dancy, 1983). The disadvantage of the relaxation method is that one wavelength is used for generating the waves and two for dissipating the waves so the NWT length is enlarged. The relaxation functions used for this zones are a combination of analytical solutions with variables from the simulation:

$$\begin{aligned} u(\tilde{x}) &= \Gamma(\tilde{x})u_{analytical} + (1-\Gamma(\tilde{x}))u_{computational} \\ w(\tilde{x}) &= \Gamma(\tilde{x})w_{analytical} + (1-\Gamma(\tilde{x}))w_{computational} \\ p(\tilde{x}) &= \Gamma(\tilde{x})p_{analytical} + (1-\Gamma(\tilde{x}))p_{computational} \\ \phi(\tilde{x}) &= \Gamma(\tilde{x})\phi_{analytical} + (1-\Gamma(\tilde{x}))\phi_{computational} \end{aligned} \tag{2.32}$$

The function $\Gamma(\tilde{x})$ varies depending on the location of the relaxation zone, transforming the values from the analytical to the computational ones. In the numerical beach zone, where the waves dissipate, the transformation of the values is from the computational to the analytical values.

In addition to the relaxation method, for the numerical beach zone, an active absorption method can be employed. Using this method, the wave dissipation zone is not needed using more length of the NWT except the wave generation zone. The active absorption produces a velocity with the opposite direction to the incoming waves so they are cancelled. Using linear long-wave theory the velocity to match the velocity of the waves to be absorbed can be obtained (Schäffer and Klopman, 2000):

$$U(t) = -\sqrt{\frac{g}{h}}\xi(t) \tag{2.33}$$

where $\xi(t)$ is the free surface elevation with respect to the mean water level measured at the absorption zone as:

$$\xi(t) = \eta(t) - d \tag{2.34}$$

where $\eta(t)$ is the actual free surface along the downstream boundary and d the still water level.

2.7.3 Wave theories

Waves are obviously one of the most significant factors in marine civil engineering. Waves can be produced by wind or gravity and depends on the water depth or the slope of the seabed. The need to know the properties of the waves is important to measure the effects they will produce. In the nineteenth century, modern theories appeared, mainly in the work of Stokes based on previous theoretical advances by Airy, Laplace or Lagrange. The wave theories used in the thesis are linear wave theory and second-order Stokes wave theory.

- The linear theory or Airy wave theory gives a linearised description of the propagation of gravity waves. Velocities for an arbitrary depth as given in Krogstad and Arntsen (2003) for horizontal and vertical velocity are:

$$u(x,z,t) = aw\frac{\cosh(k(d+z))}{\sinh(kd)}\sin(wt-kx) \tag{2.35}$$

$$w(x,z,t) = aw\frac{\sinh(k(d+z))}{\sinh(kd)}\cos(wt-kx) \tag{2.36}$$

where a is wave amplitude, $w = 2\pi/T$ is the observed wave angular frequency, $k = 2\pi/\lambda$ is wave number with λ wavelength, d is water depth, t is time and x the direction of propagation.

- The second-order Stokes wave velocities after Dean and Dalrymple (1997):

$$\begin{aligned} u = -\frac{\partial\phi}{\partial x} = \frac{H}{2}\frac{gk}{w}\frac{\cosh(k(d+z))}{\cosh(kd)}\cos(kx-wt) \\ + \frac{3}{16}\frac{H^2wk\cosh(2k(d+z))}{\sinh^4(kd)}cos(2(kx-wt)) \end{aligned} \tag{2.37}$$

$$\begin{aligned} w = -\frac{\partial\phi}{\partial z} = \frac{H}{2}\frac{gk}{w}\frac{\sinh(k(d+z))}{\cosh(kd)}\sin(kx-wt) \\ + \frac{3}{16}\frac{H^2wk\sinh(2k(d+z))}{\sinh^4(kd)}sin(2(kx-wt)) \end{aligned} \tag{2.38}$$

The presence of the second-order term increases the velocities, while varying along the wave phase $2(kx-wt)$. The horizontal velocity is higher at the crest and reduced at the trough of the wave compared to the linear wave theory. This produces an oscillating net motion or drift, pointed out by Stokes (1847) as:

$$\bar{u} = \frac{wka^2\cosh(2k(d+z))}{2\sinh^2(kd)} \tag{2.39}$$

2.8 Free surface treatment.

The free surface is obtained with the level set method as a two-phase system. The zero-contour of the level set function is set between fluids where the zero level set of a signed distance function, $\phi(\vec{x},t)$, is used to represent the interface between air and water (Osher

and Sethian, 1988). The two interfaces are distinguished by the change of sign. This results in (Peng et al., 1999):

$$\phi(\vec{x},t)\begin{cases} > 0 & if\ \vec{x}\ \epsilon\ phase\ 1 \\ = 0 & if\ \vec{x}\ \epsilon\ \Gamma \\ < 0 & if\ \vec{x}\ \epsilon\ phase\ 2 \end{cases} \tag{2.40}$$

The level set function is coupled to the flow field with a pure convection equation:

$$\frac{\partial \phi}{\partial t} + u_j \frac{\partial \phi}{\partial x_j} = 0 \tag{2.41}$$

When the level set function evolves, the level set function can loose its signed distance property. A solution is to reinitialize the level set function after every time-step. The reinitialization is based on the solution of a partial differential equation (Peng et al., 1999):

$$\frac{\partial \phi}{\partial t} + S(\phi)\left(\left|\frac{\partial \phi}{\partial x_j}\right| - 1\right) = 0 \tag{2.42}$$

where $S(\phi)$ is the smooth signed function by Peng et al. (1999):

$$S(\phi) = \frac{\phi}{\sqrt{\phi^2 + \left|\frac{\partial \phi}{\partial x_j}\right|^2 \Delta x^2}} \tag{2.43}$$

Density ρ and viscosity ν are smoothed out close to the interface by calculating the density at the cell face with a regularized Heaviside function with an interface thickness of $\epsilon = 2.1dx$:

$$\rho_{i+1/2} = \rho_1 H(\phi_{1+1/2}) + \rho_2(1 - H(\phi_{i+1/2})) \tag{2.44}$$

The level set function at the cell face is obtained using the following equation:

$$\phi_{1+1/2} = \frac{1}{2}(\phi_i + \phi_{i+1}) \tag{2.45}$$

2.9 6 DOF algorithm

The FSI calculation for the floating body is carried out in the following way. A triangular surface mesh without connectivity is created to define the geometry of the body in STereoLitography (STL) format, which excludes some information about the body like its physical properties. The geometry of the body in STL format can also be imported from a file. A ray-tracing algorithm, calculating the shortest distance to the closest triangle for

the grid point, is used to determine the intersections of the surface mesh with the underlying Cartesian grid. The level set method is used to define the boundaries. The standard reinitialize algorithm is used to obtain the signed distance properties for the level set function in the vicinity of the solid body. The forces on the surface Ω are determined for each direction *i* separately with the pressure *p* and the viscous stress tensor τ:

$$F_{i,e} = \int_{\Omega} (-\mathbf{n}_i p + \mathbf{n_i} \cdot \tau) d\Omega \tag{2.46}$$

The distance of the centre of gravity from the origin of the body grid can be determined with:

$$\mathbf{r_{cg}} = \frac{1}{m} \int_{V} \mathbf{r} \rho_a dV \tag{2.47}$$

where $\mathbf{r}$ is the distance from each surface cell to the origin of the body-fitted coordinate system. Assuming that the origin of the body-fitted coordinate system is at the centre of gravity of the floating body, $\mathbf{r}$ is the distance of each surface cell to the centre of gravity. The moment can be calculated with the following equation:

$$L_{i,e} = \int_{\Omega} \mathbf{r} \times (\mathbf{n_i} p + \mathbf{n_i} \cdot \tau) d\Omega \tag{2.48}$$

The calculation of the discrete surface area is done with a Dirac delta function:

$$d\Omega = \int \delta(\phi) |\nabla \phi| dx \tag{2.49}$$

The location and orientation of the floating body are given by the position vector and the Euler angles:

$$\boldsymbol{\eta} = (\boldsymbol{\eta_1}, \boldsymbol{\eta_2}) = (x_{cg}, y_{cg}, z_{cg}, \phi, \theta, \psi) \tag{2.50}$$

The calculation of the moments of inertia can be simplified with two different coordinate systems, one inertial for the fluid and another non-inertial for the floating body. Forces and moments can be calculated in the inertial coordinate system and when the origin of the non-inertial coordinate system coincides with the centre of gravity, the moments of inertia are calculated with a diagonal matrix:

$$\mathbf{I} = \begin{bmatrix} I_x & 0 & 0 \\ 0 & I_y & 0 \\ 0 & 0 & I_z \end{bmatrix} = \begin{bmatrix} mr_x^2 & 0 & 0 \\ 0 & mr_y^2 & 0 \\ 0 & 0 & mr_z^2 \end{bmatrix} \tag{2.51}$$

where r_x, r_y and r_z are the distance between the point and the centre of gravity in each direction x, y, z.

After, the forces and moments can be expressed in the non-inertial coordinate system with a transformation matrix $\mathbf{J_1^{-1}}$ with three rotations around each axis:

$$\mathbf{a}_{fb} = \begin{bmatrix} c\psi\, c\theta & s\psi\, c\theta & -s\theta \\ -s\psi\, c\phi\ + s\phi\, s\theta\, c\psi & c\psi\, c\phi\ + s\phi\, s\theta\, s\psi & s\phi\, c\theta \\ s\theta s\psi + c\phi\, s\theta\, c\psi & -s\phi\, c\psi\ + c\phi\, s\theta\, s\psi & c\theta\, s\phi \end{bmatrix} \mathbf{a_e} = \mathbf{J_1^{-1}} \mathbf{a_e} \tag{2.52}$$

where sin has been denoted as s and cos as c. $\mathbf{a}_{fb}$ is the vector in the reference frame of the floating body and $\mathbf{a_e}$ is the vector in the reference frame of the inertial system.

The dynamic rigid body equations can be solved with the forces X, Y, Z, momentums K, M, N and moments of inertia:

$$\begin{aligned} F_i &= \mathbf{J_1^{-1}} F_{i,e} = [X, Y, Z] \\ L_i &= \mathbf{J_1^{-1}} L_{i,e} = [K, M, N] \end{aligned} \tag{2.53}$$

with:

$$\begin{aligned} &[m(\dot{u} - \nu r + \omega q)] = X \\ &[m(\dot{\nu} - \omega r + \nu q)] = Y \\ &[m(\dot{\omega} - \nu r + \omega q)] = Z \\ &[I_x(\dot{p} + (I_z - I_y)qr] = K \\ &[I_y(\dot{q} + (I_x - I_z)rp] = M \\ &[I_z(\dot{r} + (I_y - I_x)pq] = N \end{aligned} \tag{2.54}$$

where u, v, w the linear velocities and p, q, r the angular velocities obtained before. Then $\dot{u}, \dot{v}, \dot{w}, \dot{p}, \dot{q}$ and $\dot{r}$ can be calculated in an explicit manner.

Linear and angular velocities $\dot{\varphi}$, position or orientation vector φ of the floating body can be calculated with a second-order Adams-Bashforth scheme for the new time-step:

$$\begin{aligned} \dot{\varphi}^{n+1} &= \dot{\varphi}^t + \frac{\Delta t}{2} \left(3\ddot{\varphi}^{n+1} - \ddot{\varphi}^n\right) \\ \varphi^{n+1} &= \varphi n + \frac{\Delta t}{2} \left(3\dot{\varphi}^{n+1} - \dot{\varphi}^n\right) \end{aligned} \tag{2.55}$$

The floating body dynamics are solved in a explicit way. The dynamic rigid body equations are solved in the floating body reference frame. Translations and orientations are also calculated. The transformation is done with the following matrix J_2, where sin has been denoted as s, cos as c and $\tan$ as t:

$$\dot{\boldsymbol{\eta}}_{\mathbf{2}} = \begin{bmatrix} 1 & s\phi\,/t\theta & c\phi\,/t\theta \\ 0 & c\phi & -s\phi \\ 0 & s\phi/c\theta & c\phi/c\theta \end{bmatrix} \boldsymbol{\nu}_{\mathbf{2}} = \mathbf{J}_{\mathbf{2}}\nu_{\mathbf{2}} \tag{2.56}$$

The boundary conditions for the velocities on the solid-fluid interface result from the motion of the solid body in respect to its centre of gravity:

$$u_i = \dot{\boldsymbol{\eta}}_{\mathbf{1}} + \dot{\boldsymbol{\eta}}_{\mathbf{2}} \times \mathbf{r} \tag{2.57}$$

Pressure oscillations near the solid body occurs because of solid cells turns into fluid cells and vice versa. A field extension method is implemented and adapted to the ghost cell immersed boundary method. For non-moving boundaries, a zero-gradient boundary condition is used for the pressure. The following boundary condition for the gradient of the pressure is used to maintain a physical pressure gradient near the floating body:

$$\frac{\partial p}{\partial x_i} = -\frac{1}{\rho}\frac{Du_i}{Dt} \tag{2.58}$$

To obtain u_i, Eq. (2.57) is differentiated with respect to time and used for the ghost cell values for the pressure:

$$\frac{Du_i}{Dt} = \frac{\partial}{\partial t}(\dot{\boldsymbol{\eta}}_{\mathbf{1}} + \dot{\boldsymbol{\eta}}_{\mathbf{2}} \times \mathbf{r}) \tag{2.59}$$

To avoid problems caused when a cell becomes a fluid cell and have non-physical values for velocities and pressure, velocities from Eq. (2.57) are used and the pressure is found through interpolation from the fluid.

2.10 Parallelization

REEF3D takes advantage of the progress in parallelization for computational calculations. In parallel computing, the work is split into all the processors to reduce the time necessary to converge to the solution. An example is the HYPRE library, which uses massively parallel machines for pre-conditioners and solvers which have been explained in sub-section 2.4.1. The scalability or parallelization is an important aspect in parallel computing. In the case of HYPRE, the scalability is weak which means that if the size of the problem and the number of cores are increased proportionally, the computing time remains approximately the same. REEF3D uses Message Passing Interface (MPI) for the message passing communication between processors. The domain is divided and assigned to separated processors. The adjacent cells in the divisions are shared to maintain the continuity.

THIS PAGE INTENTIONALLY LEFT BLANK.

CHAPTER 3
VALIDATION AND DISCUSSION

In this chapter, simulations results are discussed. Firstly, the 6DOF algorithm will be validated with a two-dimensional simulation of a free floating rectangular barge. Validation will be accomplished comparing numerical results with laboratory experiment results. Then, a three-dimensional simulation of the same barge will be carried out to study the effects of the wall distance on the motions of the body. Finally, a free floating ship with waves will be simulated and its motions compared with experimental data.

3.1 Two-dimensional simulation of a free-floating barge

For validation of the 6DOF algorithm, a case is set up with a rigid floating body in two dimensions under the effect of waves. The configuration and geometry of the laboratory experiment realised in Dalian University is explained in Ren et al. (2015) and will be explained following. For the simulations, Ren et al. uses a Weakly Compressible Smoothed Particle Hydrodynamic (WCSPH) method with reasonably good results. Calderer et al. (2014) studied the roll decay and vorticity produced by the rotation of a rectangular barge with a new approach of the FSI curvilinear immersed boundary method of Borazjani et al. (2008). Koo and Kim (2004) studied the motions of a freely floating-barge in a two-dimensional non-linear numerical wave tank based on the potential theory. In this simulation the REEF3D numerical model with the 6DOF algorithm explained in chapter 2 is used.

The laboratory experiment was performed in a wave flume which is 20 m long, 0.8 m high and 0.44 m wide. The floating body consists of a box or rectangular barge with a length $l = 0.30$ m and a height $h = 0.20$ m. The breadth of the box leaves a 0.01 m gap on each side. With this geometry, two-dimensional motion is looked for, restricting sway, roll and yaw. The initial position of the barge is defined by its centroid at $x, z = 2.0$ m, 0.4 m. Density of the body is $\rho = 500$ kg/m^3. The floating body is under the effect of regular

waves with wave height $H = 0.04$ m, period $T = 1.2$ s and wavelength $\lambda = 1.936$ m. The water depth in the tank is $d = 0.4$ m.

The degrees of freedom in the simulation are movement along the x and z axis and rotation around y axis, surge, heave and pitch, respectively. The simulation is carried out in a numerical wave tank with the same geometry as the wave flume. The NWT is divided in three zones where the initial wave zone is equivalent to one wavelength and the end zone or numerical beach is equal to two wavelengths. The barge is positioned at $x = 7.0$ m from the start of the tank so the wave reflection does not affect the simulation results. The centroid z-coordinate is maintained from the experiment. The water depth is the same as the experiment. The configuration is shown in Fig. 3.1 and Fig. 3.2.

To characterize the waves, second-order Stokes wave theory is used with the wave characteristics from the experiment. Surge results are expected to show the oscillatory net motion or Stokes drift. The floating body has the same dimensions and density as the experiment. The breadth of the barge is equivalent to one grid size (dx) to perform a two-dimensional simulation.

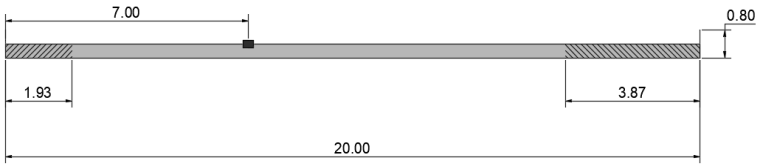

Figure 3.1: Geometry of the tank for the two-dimensional simulation. *(Dimensions in metres)*

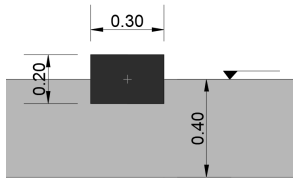

Figure 3.2: Geometry of the floating body and water depth. *(Dimensions in metres)*

The results from the simulation will be compared with the experiment. Results will be contrasted after several seconds when the series of waves stabilize, reach the body, and motion starts. Total computational time is 20 s, the matching part will be shown in the results. Different grid sizes are used for the simulation case: 0.025 m, 0.01 m and 0.005 m with a total cells of 800x60, 2000x150 and 4000x300, respectively. The grid with a better accuracy-computational cost will be used for further analysis. Results are normalised for

all the variables obtained:

$$\begin{aligned} time &= \frac{t}{T} \\ heave\ and\ surge &= \frac{result - d}{d} \\ pitch &= \frac{\theta}{k \cdot d} \end{aligned} \tag{3.1}$$

The heave results in Fig. 3.3 match the simulations after $t/T = 6.36$. The results are accurate in relation to height values except the crests between the first and second waves. The troughs are smaller except for the last oscillation at $t/T = 11$. All the grids show a good match with the experiment data as shown in Fig. 3.3a.

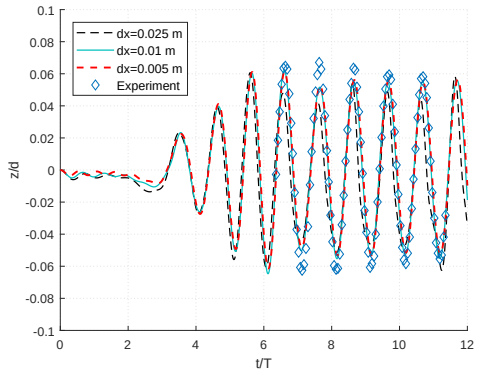

(a) All grid sizes and experiment data

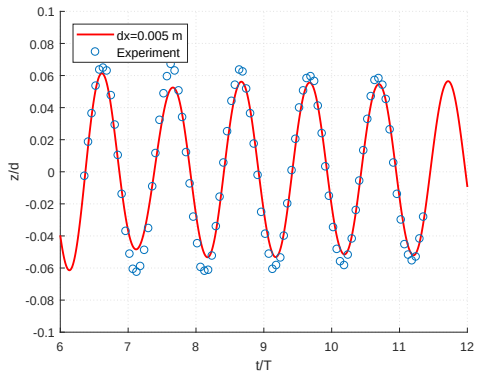

(b) dx=0.005 m and experiment data from $t/T = 6.0$ to $t/T = 12.0$

Figure 3.3: Heave motion of the two-dimensional barge with three grid sizes and experiment data in **(a)**. Heave motion with the finest grid and experiment data in **(b)**.

In Fig. 3.3b a detail of the matching part is showed with only dx=0.005 m. In the trimmed

heave Fig., it can be seen that the crests of the second and third waves are higher in the experiment. The first three troughs have a small difference compared to the experiment, while the rest match consistently. This may be due to the position of the box farer from the original position in the experiment.

In Fig. 3.4, the rotation of the box around y axis or pitch is presented. In Fig. 3.4a, all the grid sizes are shown. The deviation of the results is high from the coarser grid of dx=0.025 m to the other grids of dx=0.01 m and dx=0.005 m. The results with dx=0.025 m are out of order in the comparison. Results between the other two grids are reasonable equal with a small variation for dx=0.01 m.

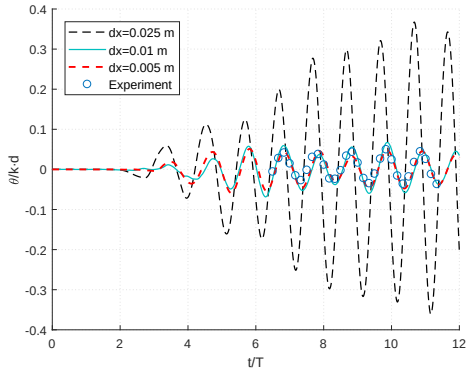

(a) All grid sizes and experiment data

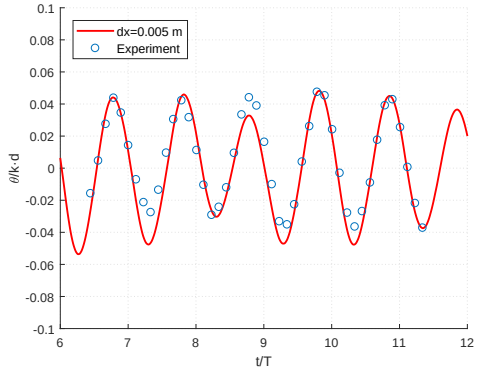

(b) dx=0.005 m grid size and experiment data from $t/T = 6.0$ to $t/T = 12.0$

Figure 3.4: Pitch motion of the two-dimensional barge with three grid sizes with experiment data in **(a)**. Pitch motion with the finest grid and experiment data in **(b)**.

In Fig. 3.4b, pitch motion between time $t/T = 6.0$ and $t/T = 12.0$ is shown with dx=0.005 m for a better view of the comparison between numerical and experiment results. The results from the software are satisfactory to a large degree but the negative rotation

between first and second wave is smaller in the experiment as well as the third positive rotation peak which is slightly higher than numerical results.

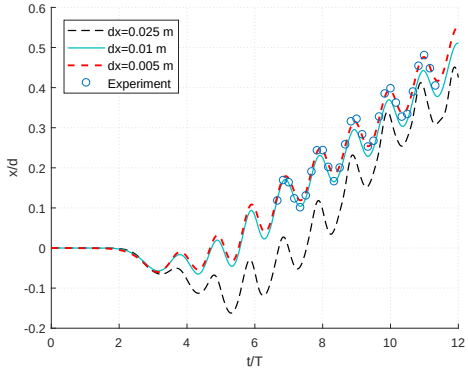

(a) All grid sizes and experiment data

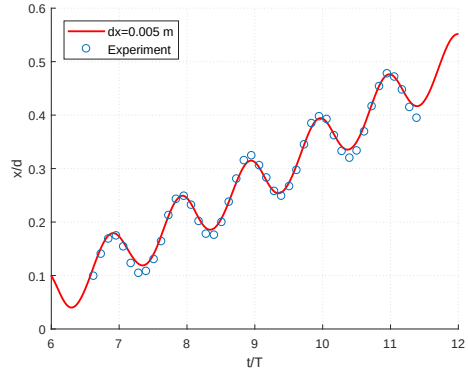

(b) dx=0.005 m and experiment data from $t/T = 6.0$ to $t/T = 12.0$

Figure 3.5: Surge motion of the two-dimensional barge with three grid sizes and experiment data in **(a)**. Surge motion with the finest grid and experiment data in **(b)**.

In Fig. 3.5, surge or movement along x axis is presented. All the cases have a negative part at the start of the simulation in Fig. 3.5a, which means that the first waves are provoking an approach to the start of the tank. After the initial negative part, the barge starts to move to the end zone of the tank in all the grid sizes. The negative surge of dx=0.025 m is significant compared to the other two grids and although the slope is close at the beginning, the results are lower in magnitude. Besides, around $t/T = 10.0$, the results are coming closer to the other grid results so the slope is changing. Grid size dx=0.01 m presents good results with a small magnitude difference with experiment results. The finest grid size matches the experiment results really well.
In Fig. 3.5b, results are shown between $t/T = 6.0$ and $t/T = 12.0$ with only dx=0.005 m and experiment data. For the surge, the simulation matches almost perfectly the behaviour

of the rectangular barge under the effect of the waves. A slight difference is seen for the troughs in the first and last oscillations.

Surge motion presents an oscillatory movement called Stokes drift represented in Fig. 3.5 due to the non-linear wave theory used, second-order Stokes wave theory. With the representation in Fig. 3.6, the trajectory of the centroid of the body, surge and heave motions for a single wave period can be seen clearly. The wave chosen is one at $t/T = 8$, although others could be used with related results. The trajectory of the centroid of the barge is showed with the surge in x-axis and the heave in y-axis. dx=0.025 m is not shown in the Fig. because of the disparity in surge seen in Fig. 3.5a.

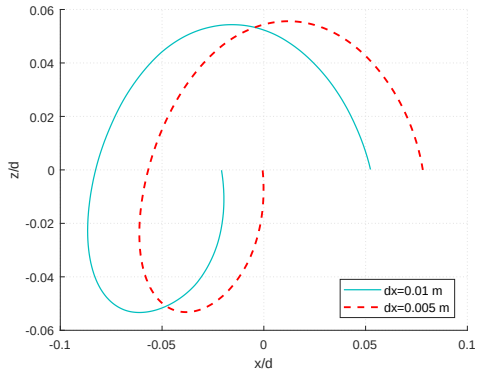

(a) Two grid sizes.

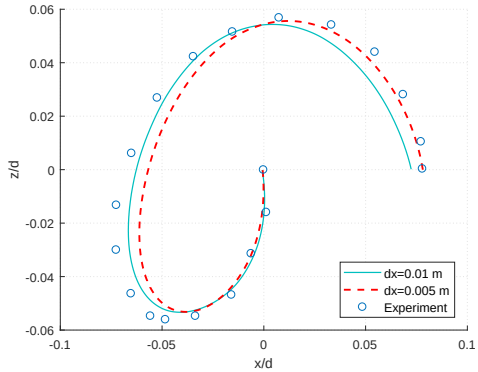

(b) Two grid sizes and experiment data. *(dx=0.01 surge modified)*

Figure 3.6: Centroid trajectory of the two-dimensional barge for a wave period T with two grid sizes in **(a)** and experiment data in **(b)**.

The mismatch in x-axis in Fig. 3.6a is due to the difference in surge magnitude between the two grid sizes, that is presented in Fig. 3.5a. Fig. 3.6b shows both grid sizes compared to experiment data. Surge results for dx=0.01 m have been modified in order to match the

origin of the coordinate system in Fig. 3.6b. In this way, both grid sizes can be compared to the experimental spiral shape.
Results show that heave motion is correct in magnitude for both grid sizes with a disagreement for the negative heave. The difference for negative heave was described before in Fig. 3.3. Surge motion presents a slight difference in the negative values, when the barge is moving to the start of the NWT for both grid sizes. The negative surge motion seems to be better described by dx=0.01 m grid size than the finest grid for this oscillation. However, it should be taken into account the magnitude difference for dx=0.01 m in Fig. 3.6a. The surge values are lower for dx=0.01 m than the finest grid which matches better the experiment results as shown in Fig. 3.5a.

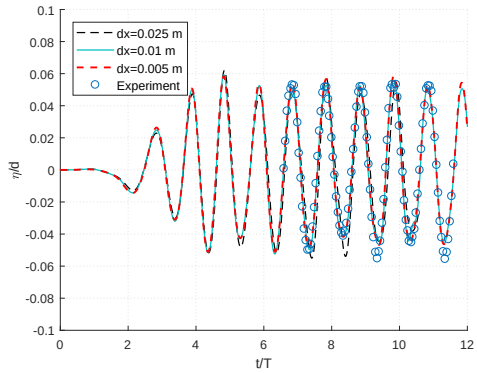

(a) Three grid sizes and experiment data

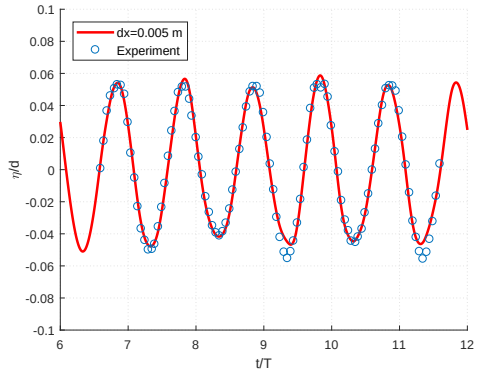

(b) dx=0.005 m and experiment data from $t/T = 6.0$ to $t/T = 12.0$

Figure 3.7: Wave elevation of the two-dimensional barge with three grid sizes and experiment data in**(a)**. Wave elevation with the finest grid and experiment data in **(b)**.

The wave elevation is presented in Fig. 3.7. In Fig. 3.7a all the grid sizes are presented. It shows a significant agreement between numerical results and experimental data for all the grid sizes. There is a disagreement in the trough of the second wave for dx=0.025 m,

which other grids represents correctly. The only mismatch for dx=0.01 m and dx=0.005 m occurs in the trough in the third and fifth wave which are slightly lower than experimental results. The detail of the mismatch can be seen in Fig. 3.7b with only dx=0.005 m and experiment results.

In order to measure the error or deviation between the simulation and the experimental data, the mean absolute error (MAE) and root mean squared error (RMSE) is calculated for each grid size. Results are shown in table 3.1 with RMSE between parenthesis. The MAE is calculated as:

$$MAE = \frac{1}{N}\sum_{i=1}^{N}|X_i - Y_i| \tag{3.2}$$

and the RMSE:

$$RMSE = \sqrt{\frac{\sum_{i=1}^{N}(X_i - Y_i)^2}{N}} \tag{3.3}$$

where N is the number of elements, X_i is the simulation value i, Y_i is the experimental value i.

It should be taken into account that both, MAE and RMSE, are calculated only for the matching part between simulation and experimental results between $t/T = 6.36$ and $t/T = 11.36$.

Grid size (m)	Wave elevation	Heave	Pitch	Surge
0.025	0.032 (0.0405)	0.048 (0.056)	0.173 (0.201)	0.093 (0.11)
0.01	0.011 (0.014)	0.009 (0.012)	0.016 (0.019)	0.021 (0.026)
0.005	0.008 (0.011)	0.010 (0.013)	0.0135 (0.017)	0.011 (0.014)

Table 3.1: Mean absolute error and root mean squared error *(in parenthesis)*. All grid sizes, wave elevation and motions.

From the results shown in table 3.1, the waves created in the middle and the finest grid sizes present similar results with small differences. The deviation for the coarsest grid size is larger. The heave motion of the middle grid presents better results than the other grids. Although, the difference with the finest grid is minor. For pitch motion, the coarsest grid is an order of magnitude higher than other grid sizes. The other grid sizes present similar results. For the surge, the finest grid presents better results. The difference with the middle grid is larger in comparison with the other motions. The coarsest grid has a high deviation. The difference between the middle and the finest grid is almost negligible for all results except surge motion. However, the number of cells created for each case is an important aspect that should be considered. The factor of cells created with a half size grid is 2^n

where n are the dimensions. Overall, the finest grid has the best results and the coarsest grid size is discarded for the pitch results. The middle grid presents excellent results for heave motion with less error with experiment results than the finest grid. For the pitch and wave elevation, the middle grid has good results with small differences with the finest grid except for surge motion.

In Fig. 3.8 the motion of the barge is presented with a time-step of $t/T = 0.5$ starting at $t/T = 6.4$. The different figures are taken from the same position which allow to check the surge motion of the barge over time. The pitch peaks almost coincide with the time-steps, showing nearly the maximum angle of rotation in Fig. 3.8b and Fig. 3.8c. Besides the horizontal velocity is shown along with the free surface. In all the Fig. a velocity change can be seen around the corners due to the pitch motion., especially in Fig. 3.8b when a wave has passed and Fig. 3.8c when the barge is close to the crest of the wave.

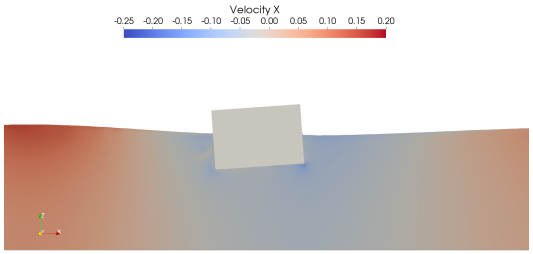

(a) t/T = 6.4

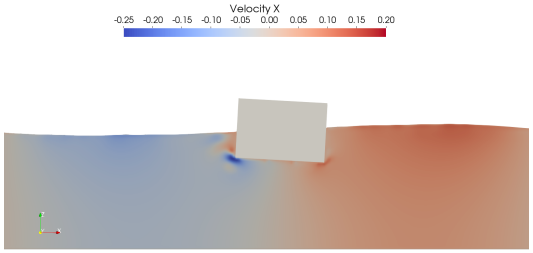

(b) t/T = 6.9

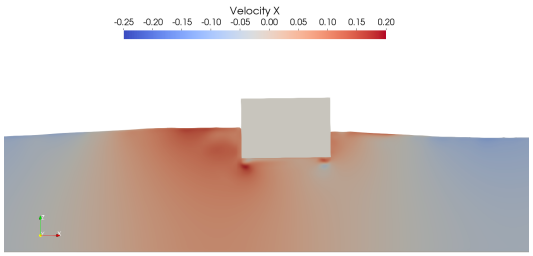

(c) t/T = 7.4

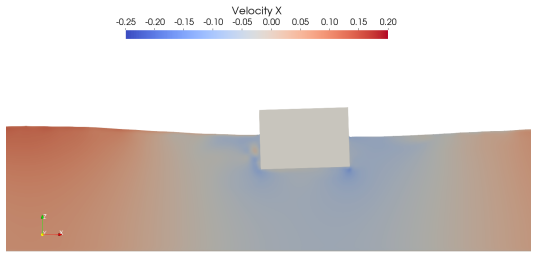

(d) t/T = 7.9

Figure 3.8: Motions of the two-dimensional barge with horizontal velocity and time-step $t/T = 0.5$.

In Fig. 3.9, the vorticity around y axis is presented with the same time-steps as Fig. 3.8. The vorticity is presented for both fluids, air above the barge and water below. On the sides, the fluids are separated by the free surface represented with a black line. Colour red represents positive vortices and blue negative vortices. Vortices seen far from the barge, on the sides and on the free surface, are due to the waves. Vortices are created around the corners when the box rotates in $t/T = 6.9$ and $t/T = 7.4$ accordingly with the velocity changes in Fig. 3.8.

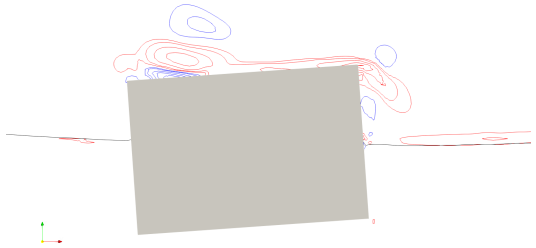

(a) $t/T = 6.4$

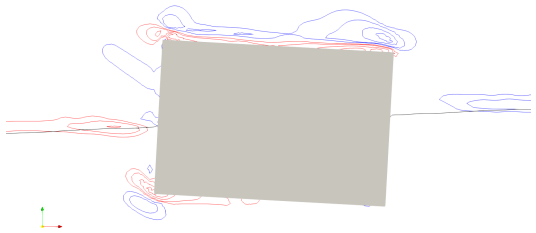

(b) $t/T = 6.9$

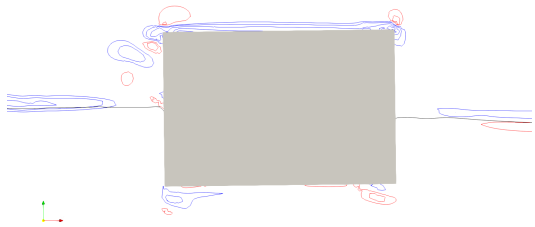

(c) $t/T = 7.4$

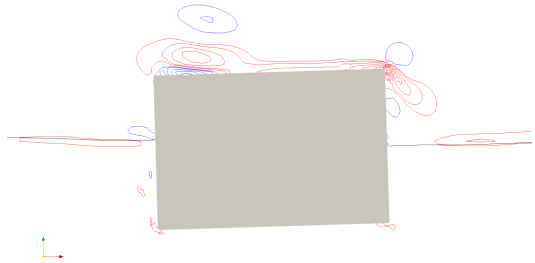

(d) $t/T = 7.9$

Figure 3.9: Vorticity y of the two-dimensional barge with $t/T = 0.5$ time-step.

The effect can be seen in Fig. 3.9b and 3.9c. These time-steps coincide almost with a rotation peak. From that instant, the barge starts rotating in the opposite direction or it reaches the maximum pitch angle. For example, in Fig. 3.9c, the barge will continue moving counter-clockwise while in Fig. 3.9b the barge is close to the maximum pitch angle.

Another wavelength has been simulated as further analysis with dx=0.01 m. The new wavelength has a value of $\lambda = 1.5$ m. The new wavelength has a difference more than one length of the body to the original wavelength of $\lambda = 1.936$ m. The geometry of the tank and the barge remain, as well as the amplitude. The period of the waves is $T = 1.01$ s. The position of the rectangular barge is also maintained. The different motions are shown from the start of the simulation until $t/T = 12$.

The heave presented in Fig. 3.10 has nearly constant values for the highest and the lowest peaks. The range goes from -0.06 to 0.06 similar to the heave motion range in Fig. 3.3 as the wave amplitude is the same. Heave results for this wavelength does not shown the lower troughs around the fifth wave as seen in Fig. 3.3a at $t/T = 8$. Due to the lower wavelength, the number of oscillations shown in the same time-step are higher.

In Fig. 3.11, the pitch motion is presented. The values are lower by a difference of 0.02 in comparison to the validation case. The pitch for this wavelength also presents a higher deviation between the maximum values in comparison to dx=0.005 m shown in Fig. 3.4b where only one wave is slightly lower. The minimum value for pitch motion is -0.03

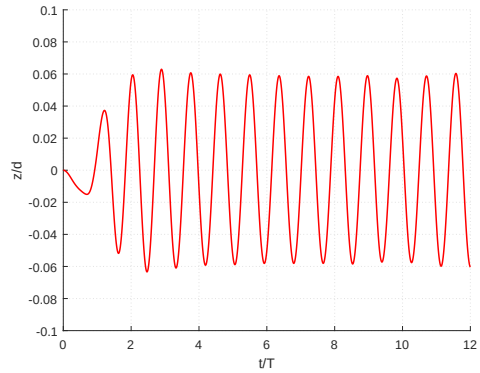

Figure 3.10: Heave motion of two-dimensional barge with $\lambda = 1.5$ m

which is smaller than the validation case with -0.04. The difference is due to the shorter wavelength with same wave amplitude.

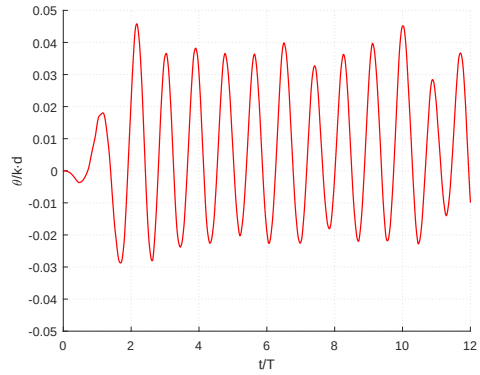

Figure 3.11: Pitch motion of two-dimensional barge with $\lambda = 1.5$ m

In Fig. 3.12, the surge motion for a wavelength $\lambda = 1.5$ m is presented. More waves are reaching and moving the rectangular barge for the same time of simulation so the displacement is higher accordingly. The first aspect noticed is the slope of the motion, which is quite higher than the surge result in Fig. 3.5 provoked by the difference in the wavelength. The initial negative part of the surge is significantly smaller than the cases from the validation shown in Fig. 3.5. Besides, the surge motion starts after $t/T = 2$ in Fig. 3.5 compared to Fig. 3.12 where the surge starts before $t/T = 1$.

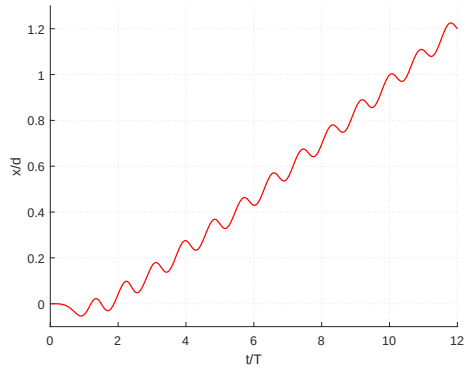

Figure 3.12: Surge motion of two-dimensional barge with $\lambda = 1.5$ m

3.2 Three-dimensional simulation of a free-floating barge

In this section, the three-dimensional simulation of the barge with the same wave conditions as the case presented in section 3.1 is carried out. The experiment in section 3.1 tried to simulate two-dimensional conditions leaving a small gap to the flume wall. However, the distance from the floating body to the wave flume wall has an effect on the results. Turbulence and water flow in the space between the barge and the tank walls will affect the free-floating motion. A ship in an inlet channel of a port would be an example of the effect of the distance with the boundary. Three cases with different wall distances will be simulated, in order to discern the effects that it has to the motions.

	Case A	Case B	Case C
Tank width (m)	0.2	0.3	0.5
Centre of gravity Y axis (m)	0.1	0.15	0.25

Table 3.2: Tank width and position of the barge in y axis of the three-dimensional barge.

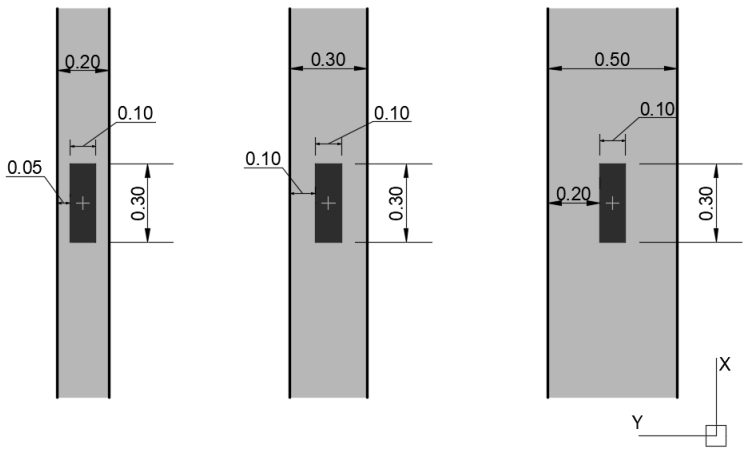

Figure 3.13: Geometry of the floating barge and numerical wave of the three-dimensional simulation. Case A, case B and case C. *(Dimensions in metres.)*

The length of the NWT is 20.0 m and the height 0.8 m. The width of the tank varies defining three cases shown in Table 3.2. The breadth of the barge is $b = 0.1$ m for all the cases. The length and height remain from section 3.1 as $l = 0.30$ m and $h = 0.20$ m, respectively. The geometry of the body, tank width and wall distance for each case is presented in Fig. 3.13. The position of the barge is defined by its centroid at $x = 7.0$ m and $z = 0.4$ m. The y-coordinate of the barge is set in the middle of the tank for all cases, shown in Table 3.2. The density is $\rho = 500.0$ kg/m^3 and the water depth is $d = 0.4$ m, same as the two-dimensional case. The wave conditions also remains from section 3.1.

The grid size used for all cases is dx=0.01 m. The choice of the grid size is explained by the accuracy achieved in the two-dimensional simulation shown in table 3.1. In comparison to dx=0.005 m, the differences are small in contrast to the cells created for each grid size. A grid of dx=0.005 m creates eight times more cells than dx=0.01 m for a three-dimensional simulation, increasing greatly the computational needs. With dx=0.01 m grid size, the total cells are 2000x20x80, 2000x30x80 and 2000x50x80 for case A, B and C, respectively. Results from the cases will be compared with two-dimensional 0.01 m grid size results and between them.

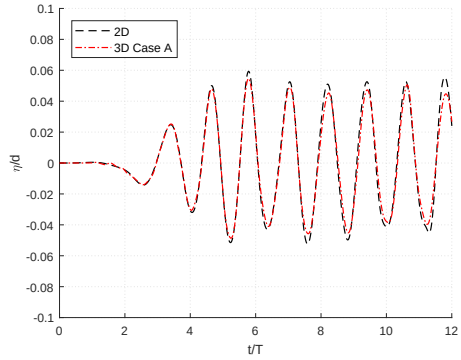

(a) Wave elevation of case A and two-dimensional case.

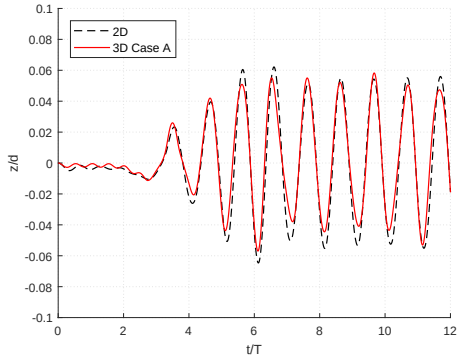

(b) Heave motion of case A and two-dimensional case.

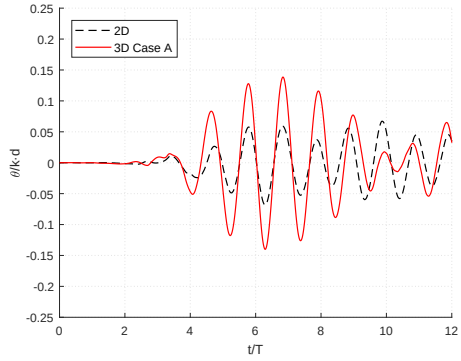

(c) Pitch motion of case A and two-dimensional case.

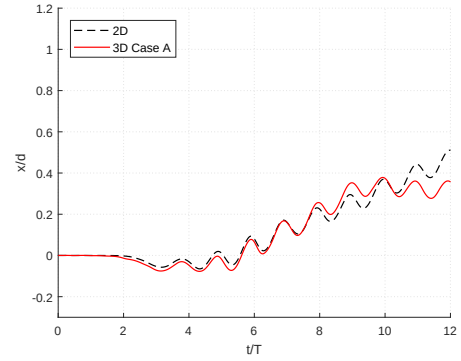

(d) Surge motion of case A and two-dimensional case.

Figure 3.14: Wave elevation and motions of the barge. Three-dimensional case A and two-dimensional case with dx=0.01 m.

In Fig. 3.14, case A is compared with the results from the two-dimensional simulation with dx=0.01 m. Case A has a tank width of 0.2 m with a gap of 0.05 m on each side of the barge.
In Fig. 3.14a, the wave elevation is presented. There are some mismatches between the

waves generated in case A and the two-dimensional case with slight differences in the troughs of the fourth and fifth wave. The crests, in general, are smaller with little disagreement after the first wave. The crest of the last wave has a larger mismatch than others. The heave motion, in Fig. 3.14b, shows that the motion is similar between case A and two-dimensional results. There is a difference in the troughs which are larger for the two-dimensional case. The crests present good results with a small disagreement for the third and fourth waves, and the last oscillation. The pitch is presented in Fig. 3.14c. The pitch for case A is large in magnitude in comparison with the two-dimensional simulation. The highest values from case A are around three times higher for positive and negative values. In the rotation at $t/T = 10$, a mismatch in time starts. A small rotation that does not match two-dimensional results. For the surge in Fig. 3.14d the first oscillations match until the fifth wave when case A changes. It should be noted that after the fifth wave, the pitch motion is also affected. This alteration may be due to the reflected wave to the barge. The slope is changing to a negative one. From that moment, the barge starts heading to the start of the tank. The Stokes drift will be present, either to the start or the end of the tank as the wave theory used is second-order or non-linear. From case A, it seems that a small wall distance affects largely the pitch motion. Heave motion result is similar and surge agrees until the fifth oscillation at $t/T = 8$.

In Fig. 3.15, case B and two-dimensional results with dx=0.01 m are compared. Case B has a tank width of 0.3 m. The space between the tank wall and the barge is equal to the barge breadth, 0.1 m.
Waves generated in case B match to a large degree the waves from the two-dimensional simulation. It is presented in Fig. 3.15a. Differences are detected in the fourth and fifth trough. Crests are marginally higher after the second wave with a larger difference in the last crest. Fig. 3.15b shows the heave motion. It has small dissimilarities with the two-dimensional case. Principally, troughs are smaller for case B. There are some, likewise, shorter crests but the match is better than troughs. There is a phase change represented with a slope variation around $t/T = 7$, at the trough. The pitch motion is presented in Fig. 3.15c being comparable to the two-dimensional case. The magnitudes values are alike between the cases shown. The maximum difference is between the peaks at $t/T = 8$. In general the case B has higher values except at $t/T = 11$ when the two-dimensional pitch is larger than case B. The changes in the rotation direction agrees well. Surge comparison in Fig. 3.15d has a small magnitude difference with two-dimensional result. However, the slope coincides between the two cases. At the end, the slope for case B increases leading to a faster displacement in x direction than the other case. This surge change is not seen in the other motions, like in Fig. 3.14 where a change was related between pitch and surge. Case B results show that a wall distance equal to the body breadth has an influence on pitch and surge motion. In pitch, the values are higher but the effects seen are limited. In surge, the displacement is similar with a small magnitude difference.

In Fig. 3.16, case C and two-dimensional results are compared. The tank width is 0.5 m with a gap of 0.2 m, two times the body breadth.
In Fig. 3.16a, the waves from both cases are compared. The results are similar with a mismatch for the crests values that are lower for case C. Moreover, there are differences in the troughs for the fourth and fifth wave. Heave motion, in Fig. 3.16b, presents dis-

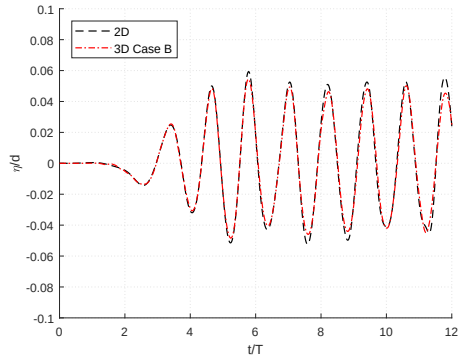

(a) Wave elevation of case B and two-dimensional case.

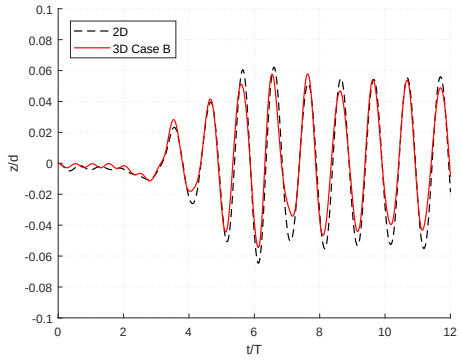

(b) Heave motion of case B and two-dimensional case.

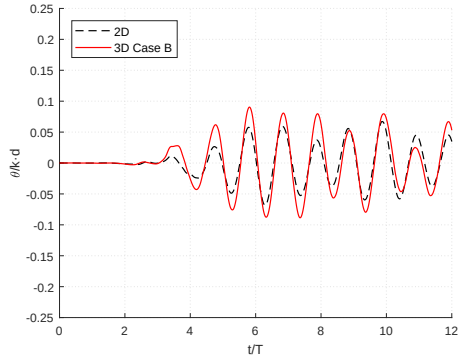

(c) Pitch motion of case B and two-dimensional case.

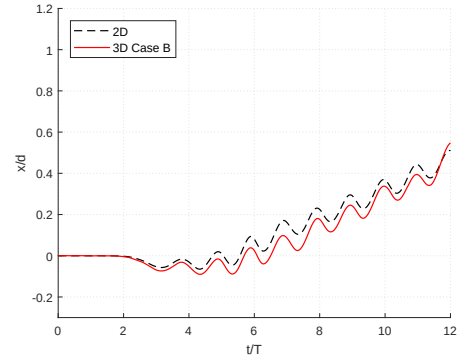

(d) Surge motion of case B and two-dimensional case.

Figure 3.15: Wave elevation and motions of the barge. Three-dimensional case B and two-dimensional case with dx=0.01 m

similarities in the troughs magnitude. The crest of the third, fourth and last wave is also lower. There is a slope change at the fourth oscillation at the trough. After the oscillation at $t/T = 8$, a slight time difference is observable between both cases. In Fig. 3.16c, the pitch motion shows results with values more than double than the two-dimensional case for the maximum values. Furthermore, pitch also shows a time difference for the last rotations, after $t/T = 8$. The last rotation is shorter, not following the two-dimensional case. In Fig. 3.16d, surge comparison is presented. The surge for case C is completely different than two-dimensional heave motion. For surge, the time difference is perceptible in the fifth oscillation at $t/T = 8$. Results with a wall distance larger than the breadth show that all the motions are affected. Heave is affected with small differences, however pitch and surge results are quite different than two-dimensional pitch and surge. The time difference may be explained by a wave reflection affecting the body motion.

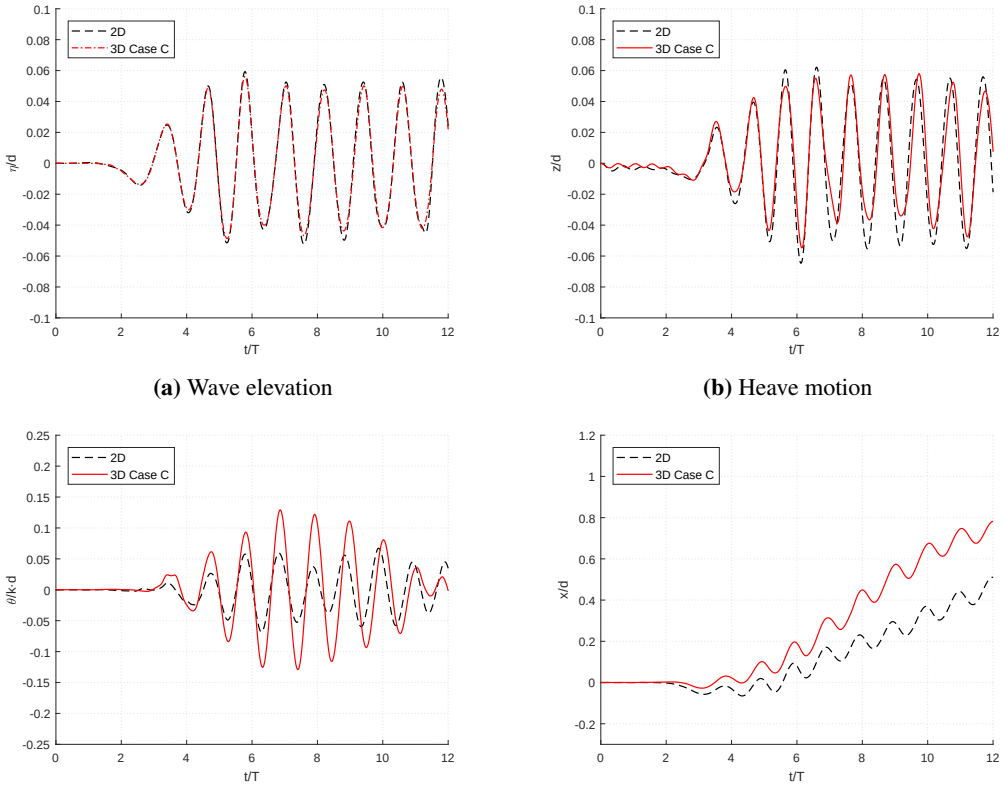

(a) Wave elevation

(b) Heave motion

(c) Pitch motion

(d) Surge motion

Figure 3.16: Wave elevation and motions of the barge. Three-dimensional case C and two-dimensional case with dx=0.01 m

After comparing the cases with two-dimensional results, the three cases are compared between them.

In Fig. 3.17, the wave elevation is presented. The wave height match among cases confirming that all cases have the same wave conditions. The waves generated are consistent. A negligible difference is observable in case A in the last two waves generated at the troughs. Cases B and C present coincidental results.

Fig. 3.18 shows the comparison for heave motion of the barge. All cases start with a little heave motion which was also presented in the two-dimensional case in Fig. 3.3a. However, the perturbation was slightly smaller in the validation case. Heave motion is similar between all the cases. Case A match to a large degree with case B. Case C shows smaller troughs than other cases after $t/T = 8$. Also, there is a slope change that the other two cases don't present at $t/T = 8$. At that time, occurs the time difference with the two-dimensional case, discussed before and shown in Fig. 3.16. The time difference is also noticeable with case A and case B. Heave motion is considerably approximate for all the

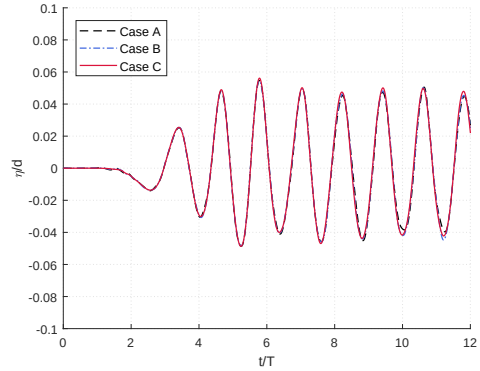

Figure 3.17: Wave elevation of all three-dimensional cases.

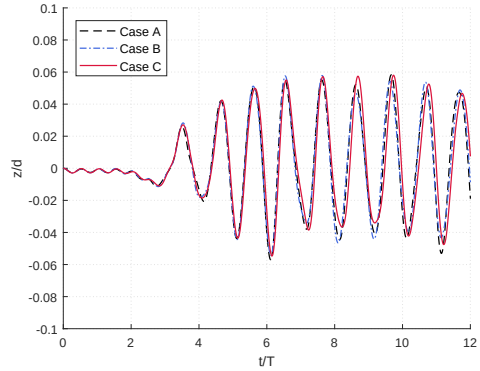

Figure 3.18: Heave motion of all three-dimensional cases.

cases so the space between the barge and the tank walls doesn't affect largely this motion. The only difference occurred in case C when the wall distance is larger than the breadth. This difference is noticeable after five oscillations. However, the mismatch starts in the fourth oscillation. Even if the time difference was caused by the reflected wave, the other cases don't present it. Cases A and B are alike, therefore a wall distance equal or less than the breadth of the floating body presents comparable heave motion results.

Pitch motion comparison is shown in Fig. 3.19. Cases A and C present the highest values for pitch. Case A begins with the highest values and decreases fast in the middle of the time shown at the fourth rotation. It has a shorter rotation at $t/T = 10$ that neither case B or case C present. Cases B and C have a similar motion at the start of the simulation for the first two rotations. However, case B results are smaller and more constant for all the simulation time. Case C presents the less diminution in pitch. Case A which presented the highest values reduces and coincides with case C at $t/T = 8$. From there, case C results are the highest. Similarly to case A, case C shows a shorter rotation a little after, at $t/T =$

11. It is noticeable that for cases with an equal or larger than breadth gap, B and C, the pitch motion almost concurs for the first two rotations. In the same way, cases with smaller or larger than breadth gap, A and C, coincide at $t/T = 8$. Then case A starts diminishing the pitch motion. From the results, it is interpreted that the smallest wall distance produces higher pitch motion but decreases quickly along time and faster than other cases. When the wall distance is the same as the body breadth, results are more constant with less deviation for the peaks. For the case with a wall distance higher than the barge breadth, the pitch motion is fairly similar to the middle case in the beginning but it increases considerably. Nevertheless, near the end of the time shown after $t/T = 9$, pitch values are similar to case B. The wall distance and the flow in the gap, affects largely the rotation of the body.

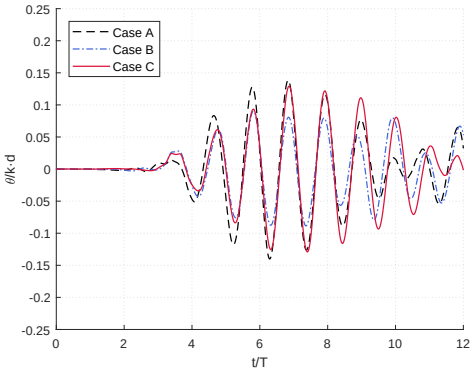

Figure 3.19: Pitch motion of all three-dimensional cases.

In Fig. 3.20, surge motion comparison is presented. Cases A and B start with a larger negative surge motion where the barge is coming closer to the wave generation zone because of the drift. Both cases present a similar negative surge in contrast to case C. The slope between cases A and B is similar before $t/T = 9$ although there is magnitude difference. Then, case A changes to a horizontal slope, possibly, due to the reflected wave. Case B, at the end of the time shown, present a larger oscillation in magnitude which might be because of the reflected wave as well. Case C has a completely different surge motion than the other two cases. Besides, the period of oscillations for case C changes after $t/T = 8$. Surge motion seems to be largely affected by the wall distance. The first noticeable point is that when the wall distance is higher than the breadth, the surge motion is much higher. This may be linked to the larger area around the sides of the body. The area is bigger so the effects impeding the surge motion spread and they are smaller. For cases with less or equal to breadth wall distance, the results are to some extent similar. The case with less wall distance than breadth, the displacement is faster and in the end, results were affected by the wave reflection or the geometry configuration.

To clarify the effects of wall distance and differences among the cases, in Fig. 3.21 the floating body is presented with the horizontal velocity x. The surge and pitch can be seen in the Fig. The range of velocities is the same for all the cases so the velocities can be compared. The images are taken from the top of the tank showing the plane x-y, with

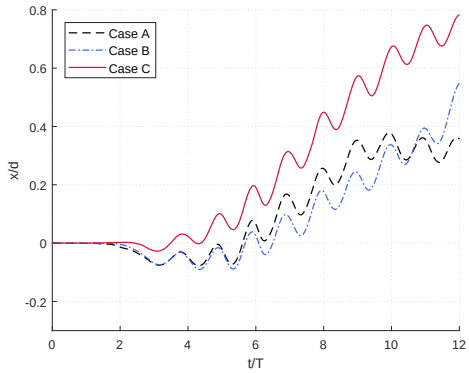

Figure 3.20: Surge motion of all three-dimensional cases.

x pointing to the right, y pointing upwards and z completing the dextro-rotatory system. The time-step is $t/T = 0.25$ starting at $t/T = 6.4$, before the fourth wave reaches the body. The Fig. is divided in four groups with the same time-step in each. The same case is placed in line. In this way, differences between cases are seen in column and the progression of the motions for every case in row. This allows to check the motions of the barge over time for a single case, and compare among cases. In the first group in Fig. 3.21a, the body is between the crests of two waves. In the second group in Fig. 3.21b, the wave crest is reaching the body. In the third in Fig. 3.21c, the wave is passing along the body, and in the last Fig. 3.21d, the wave has passed the barge and it is separating from it.

In Fig. 3.21a, it can be seen that behind the body there are two nearly zero velocities curves. Also, in front of the body there is a bulb with near-zero velocities which spreads wider than the body for cases A and B. In case C, the width of this area is narrower than the breadth. Downstream the body there are some differences. Case A present the highest velocity for the outgoing wave with a blurred dark red area. Case B has two defined lines with higher velocities which seems the wake from the body. Case C presents uniform velocities along the width of the tank. When the waves have already passed the body, the flow diverges. For case A, it seems that there is not enough space to spread. In case B, the diversion is seen with the wake lines and in case C the effect is not noticeable.
In the next time-step, Fig. 3.21b, the wave is reaching the body. All cases present a high velocity area in front of the body with similar shape. In case A, the arriving wave crest presents two curves due to the effect of the body. For case B, these two curves are more defined. In case C, this effect is seen as a fluctuation of the front of the crest. Besides, the velocity around the corners behind the body is smaller in comparison for cases A and B where a red area is seen.
When the wave is passing the body in Fig. 3.21c, lower velocities appear in front of the body due to reflection against the front of the barge. The shape is not clearly defined for case A but in case B it is seen as two round areas with blue colour. There is more width to diverge the reflection. Case C presents a more widespread and rectangular area instead of two curves. Behind the body, the maximum velocities appear near the end of the body with

two curves around the corners that are clearly seen in cases B. A similar wake from the body with two lines is seen for case B as in Fig. 3.21b. In addition, now case A presents a blurred area similar to Fig. 3.21a with near-zero velocities instead of high velocities. The narrow tank does not let the separated wakes from case B spread combining them in the same area.
In the last time-step shown, when the wave has passed the body in Fig. 3.21d the front part of the barge present a high velocity area pushing the body and making it rotates. The wave trough is seen as the dark blue area in front of the body. The shape of the area varies for each case. In case A, there is not enough space so it does not separate in two parts which can be seen in case B with a horizontal line of almost zero velocities in the middle. In case C it is seen as two separated dark blue areas. The bigger area permits the reflection of the body to spread to the entire width. Behind the body, the flow pass it and part of the flow converges to the centre. In case C, a semi-circular area with nearly zero velocities is seen behind the body. For case A, the effect is not clear, and for case B, the extent of it is not as large as case C. For case A, the velocities behind are higher as the gaps are smaller and velocities increase more than the other two cases. It can be seen that cases B and C present lighter colours than case A meaning lower velocities.
Depending on the distance between the body and the tank wall, the velocities present different values and behaviours. The width and therefore the wall distance is an element affecting the motions. Depending on the area on the sides of the floating body, velocity and other effects can spread and decrease. The wall distance affects the body motions and the reflection from the body to the incoming waves also changes depending on the tank width.

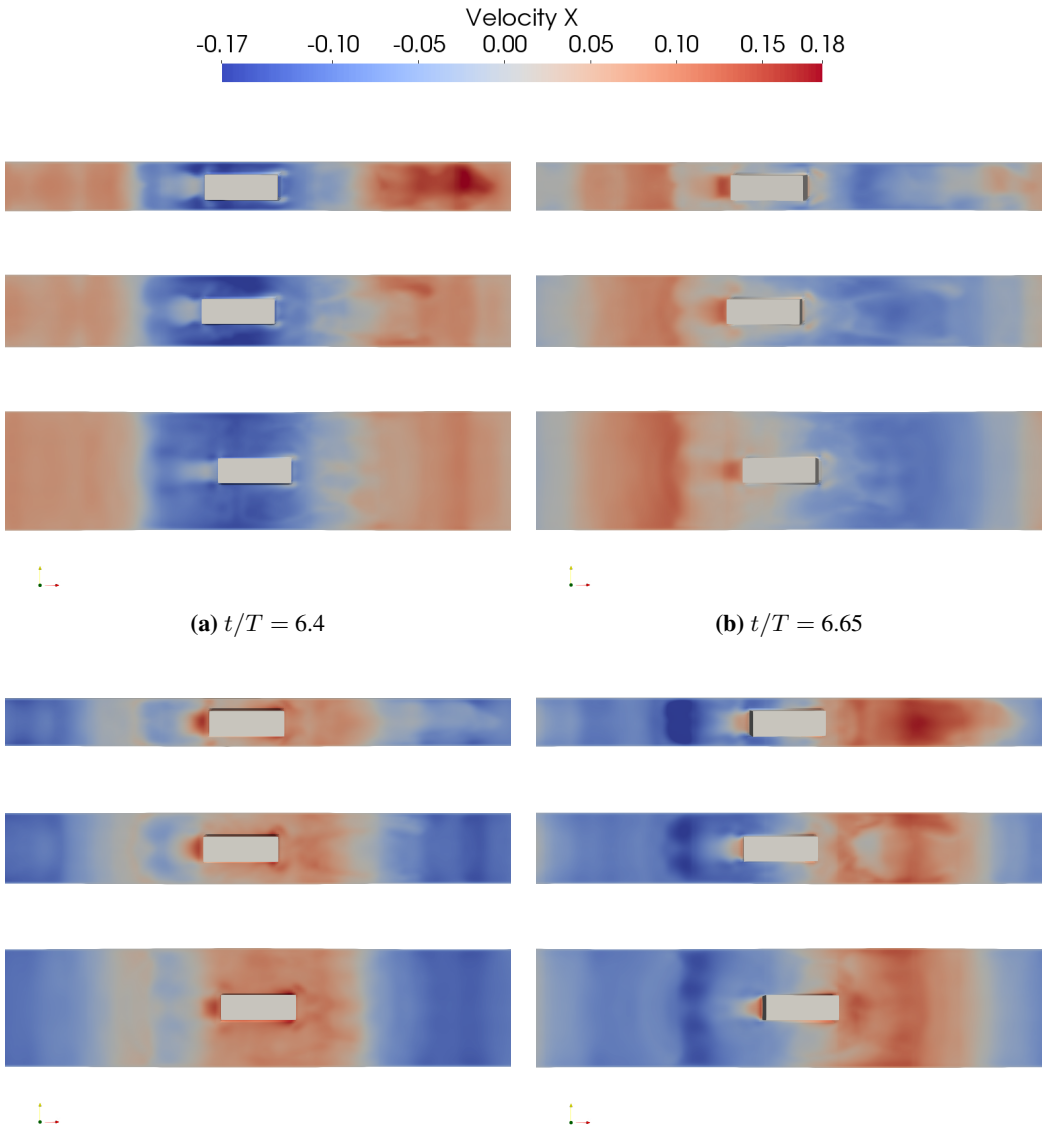

(a) $t/T = 6.4$ **(b)** $t/T = 6.65$

(c) $t/T = 6.9$ **(d)** $t/T = 7.15$

Figure 3.21: Motions of the three-dimensional barge with horizontal velocity x and time-step $t/T = 0.25$.

3.3 Three-dimensional simulation of a free-floating ship

A three-dimensional simulation of a free-floating ship in waves will be carried out in this section. The validation will be carried out comparing the numerical results with Irvine et al. (2008) for heave and pitch motions. The ship is David Taylor Model Basin (DTMB) 5512 which is a 1:46.6 scale geosim of DTMB model 5415. This model is a scale model of a US Navy's surface combatant. DTMB 5512 has been extensively studied using it for Experimental Fluid Dynamic (EFD) benchmarks for CFD validation. Yoon (2009) investigated the forces, moments and motions when the ship is manoeuvring, Longo et al. (2007) studied the diffraction problem when the ship is restricted from all the motions and advancing in waves. Carrica et al. (2007) used the EFD data for the simulation of the ship heave and pitch motions in regular waves with an URANS approach using a single-phase level set with dynamic overset grids. Shen and Wan (2013) also studied the heave and pitch motions of the ship with a volume of fluid approach and dynamic deformation mesh methods. The EFD data of the diffraction problem was also used for simulations by Carrica et al. (2006).
The experiment set-up is explained in Irvine et al. (2008). The tank is 100 m long, 3.048 m wide and 3.048 m deep. Before studying the heave and pitch motions in waves, the ship is ballasted in the paper to obtain the correct mass of the model. A summary of the particulars of the model is shown in table 3.3.

Parameter	Units	DTMB 5512
Scale ratio	-	1/46.6
Length (L_{pp})	m	3.048
Beam (B)	m	0.405
Draft (T)	m	0.132
Mass (m)	kg	86.6
Wetted surface area (S)	m^2	1.371
Block coefficient (C_B)	-	0.506
LCG	m	1.536
VCG	m	0.162
Pitch radius of giration	m	0.762

Table 3.3: Summary of DTMB 5512 particulars.

The ship is fixed to a carriage and a wave gauge is positioned to measure the wave elevation 3 m in front of the ship centroid. The distance is enough to assure that the waves are not perturbed by the ship motion. The DOF are heave and pitch. To let the unsteady free surface to develop, data acquisition starts after a series of waves travel across the length of the tank. The waves used are linear with a wave height of $H = 0.072$ m, wavelength of $\lambda = 4.57$ m and a wave period of $T = 1.712$ s.

The configuration of the case from Irvine et al. (2008) will be used for the simulation where the ship is still with free heave and pitch motion in waves. However, the numerical set-up will differ from the experimental arrangement concerning the tank geometry. The

NWT used is 8 m long, 3 m wide and 4 m high. The water depth used is $d = 2.5$ m. The wave theory used for the simulation is intermediate depth as the water depth is not mentioned in the laboratory paper. However, a depth enough to assure deep water theory is used following the rule of thumb $d/2 > \lambda$. The height of the physical tank is enough to assure deep water theory. Besides, the environment where a ship usually moves is deep waters. The wave gauge is situated 3 m in front of the centroid of the ship. Fig. 3.23 shows the geometry of the NWT. The wave generation length is equivalent to one wavelength. The relaxation zone is an active absorption beach explained in subsection 2.7.2. The ship is placed at $x = 4$ m and $y = 1.5$ m defined by its centroid. The z coordinate is located by the centroid 0.03 m above the water surface.

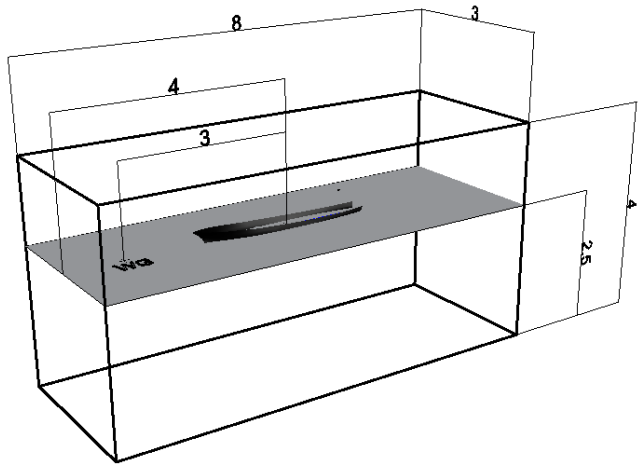

Figure 3.22: Numerical wave tank set-up and ship.

The encounter frequency is important for ships. The frequency of the waves as the ship encounters them is different from the natural wave frequency. Although, for this case with a still ship, the encounter frequency is equal to the wave frequency, which is $f = 1/T = 0.584$ Hz.

The ship geometry is imported from a STL file. The geometry definition depends on the grid size chosen for the simulation as the level set method defines the boundaries of the floating body. As an example, a dx=0.05 m, dx=0.025 m and dx=0.01 m grid is shown in Fig. 3.23 with the perfect geometry in Fig. 3.23a. In Fig. 3.23b it can be seen that the bulbous bow is separated from the body for dx=0.05 m grid affecting seriously the hydrodynamics of the ship. With a finer grid size in Fig. 3.23c, the general shape of the ship is correct but the bow still shows minor differences. Fig. 3.23d presents 0.01 m grid size geometry where the shape of the bow is almost perfect, agreeing with the geometry in Fig. 3.23a. For this reason, dx=0.01 m grid should be chosen for the simulation. Nevertheless, the number of cells created with this grid size would be 96 millions for the case. The simulation would demand really high requirements. dx=0.025 m grid showed a general good shape and the cells created will be 320x120x160 with a little more than 6 million

(a) DTMB 5512 geometry

(b) DTMB 5512 with dx=0.05 m

(c) DTMB 5512 with dx=0.025 m

(d) DTMB 5512 with dx=0.01 m

Figure 3.23: DTMB 5512 geometry in **(a)** and level set method geometry using different grid sizes.

cells. The number of cells with dx=0.025 m is more reasonable compared to dx=0.01 m. The convergence and accuracy of the 6DOF algorithm and software have already been demonstrated in section 3.1.

Next, the results will be presented and discussed. Results are shown from $t = 0$ s to $t = 12$ s. The grid size used should be taken into account with reference to section 3.1 and results with dx=0.025 m.

Fig. 3.24 shows the waves comparison between the simulation and the experiment. The agreement is very good with little differences in the troughs. The software gives better results for linear waves than second-order Stokes waves shown in Fig. 3.7.

In Fig. 3.25, heave motion is shown. The match with experimental data occurs in the second oscillation. The troughs for the numerical results are lower but all the crests match except the fourth. At $t = 10$ s a numerical error seems to occur when a perturbation or instability happened. The heave motion describes a sudden variation in a short time. However, the simulation recovers from the disturbance and continues. After this, results still agree with the experimental data without noticeable changes.

Fig. 3.26 presents the pitch motion. The pitch motion presents an agreement with the troughs values, however the crests are smaller. The pitch motion shown in Fig. 3.4a showed several order of magnitudes of difference with experimental values. Nevertheless, here, pitch motion for the same grid size presents a good agreement. The order of magnitude is correct in this case. The wave theory used is different and could one of the causes.

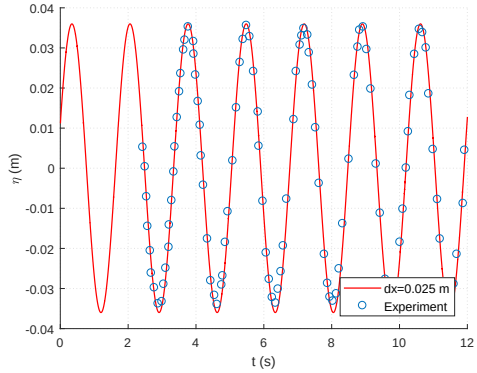

Figure 3.24: Wave elevation of the three-dimensional ship.

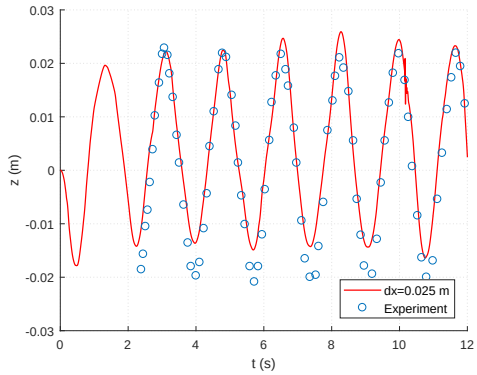

Figure 3.25: Heave motion of the three-dimensional ship.

In this case, the wave theory is linear and for the case shown in Fig. 3.4a is second-order Stokes. Besides, surge is restrained in this simulation which is allowed for the case in section 3.1.

Fig. 3.27 shows the motion and horizontal velocity x of the ship. The velocity is the same for all the Figs. The Figs. are taken from the same position. The x axis points to the right and the z axis upwards. The Fig. shows a wave period T starting at $t = 2.4$ s when numerical results match the experiment results until $t = 4.1$ s. In Fig. 3.27a the ship is between two waves. The alteration produced on the free surface is due to the damping of the stern of the ship. It can be seen in the Fig. as circles around the hull. In Fig. 3.27b the ship starts going up the wave, continuing in Fig. 3.27c when the front of the wave is modified as the bow of the ship pass the wave. Fig. 3.27d shows a better view of the modified wave crest velocity. Besides, the maximum heave and pitch motion is reached, as the ship is on top of the crest. In Fig. 3.27e the ship has passed the wave and starts the negative heave and pitch motion. The alteration of the free surface starts developing on the stern

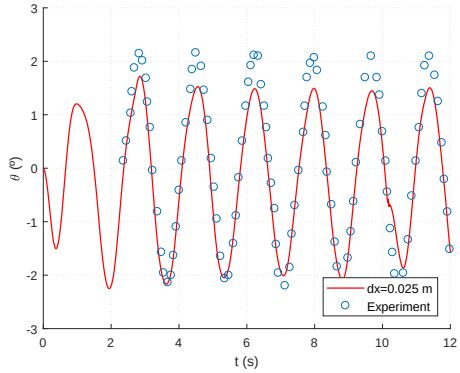

Figure 3.26: Pitch motion of the three-dimensional ship.

continuing in Fig. 3.27f. In Fig. 3.27g the minimum heave and pitch motion is reached and the wakes of the ship starts spreading. Fig. 3.27h shows a position similar to the initial between two waves. The free surface is disturbed more than in Fig. 3.27a. The effects on the free surface produced by the ship are not large in comparison to those shown in section 3.2. The reasoning is that in section 3.2 the floating body was a rectangular barge whose hydrodynamic geometry is not good. In this case, a real ship is simulated which is supposed to sail. The bow cuts the water reducing the resistance of the hull. Also, the stern is higher so the damping produced is lower when the ship is going up the wave. The geometry is optimised for its purpose.

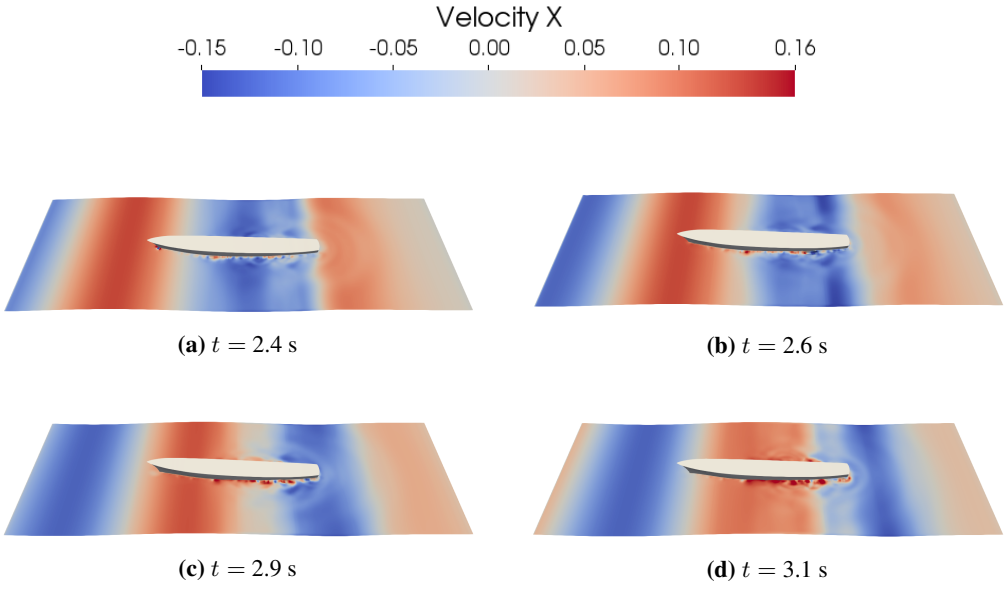

(a) $t = 2.4$ s

(b) $t = 2.6$ s

(c) $t = 2.9$ s

(d) $t = 3.1$ s

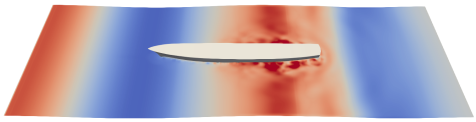

(e) $t = 3.4$ s

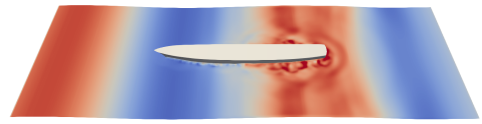

(f) $t = 3.6$ s

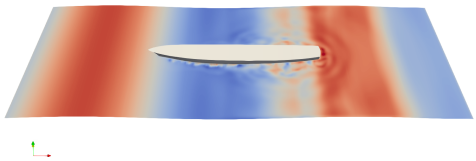

(g) $t = 3.9$ s

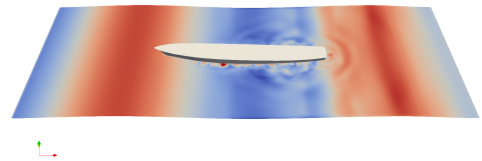

(h) $t = 4.1$ s

Figure 3.27: Three-dimensional ship motions with horizontal velocity x for a wave period T from $t = 2.4$ to $t = 4.1$ s.

THIS PAGE INTENTIONALLY LEFT BLANK.

CHAPTER 4
CONCLUSIONS AND OUTLOOK

In this chapter, the conclusions of the thesis and the future outlook are presented.

4.1 Conclusions

In this thesis, the floating body algorithm implemented in REEF3D has been explained, validated and tested for different cases. Three cases have been analysed: a two-dimensional floating barge, a three-dimensional floating barge and a three-dimensional ship.

The two-dimensional case has been studied as a validation case of the 6DOF algorithm with different grid sizes. The wave theory used was non-linear, second-order Stokes wave theory. The study with different grid sizes was used to obtain a balance between accuracy of the results and computational cost. The results agree very well with experimental data for all the different motions for the middle and finest grid sizes. Waves generated by the software presented a good agreement with the experimental data for all grid sizes. It has been noted that the results for the coarsest grid of dx=0.025 m were out of magnitude or had a big difference for pitch and surge motion. Additionally, the grid of dx=0.01 m presented remarkably good results in comparison to the finest grid dx=0.005 m. dx=0.01 m showed even better results than dx=0.005 m for heave motion. So, further analysis with a different wavelength has been carried out with dx=0.01 m.

Next, the three-dimensional case of the same barge was simulated to discern the effect of wall distance on the motions. A barge with the the same wave conditions was used for the case. The tank width was modified to create three different cases. The breadth of the barge was the same for all the cases. A comparison with two-dimensional dx=0.01 m and between the cases was realised. Results showed that the wall distance has certainly an effect on the floating body motions. Heave motion was not largely affected by the wall distance for any of the cases with a good match between them and with the validation

case. In pitch motion, the comparison with the two-dimensional case showed that a wall distance equal to the breadth of the body showed more alike results. A smaller or larger distance, presented different results to the two-dimensional case. With a smaller distance, the pitch is larger with a small decrease over time, while for a larger distance the pitch starts with high values and it decreases fast over time. The surge motion showed that a gap between the body and the tank wall equal or smaller to the breadth has similar surge motion to the validation case. A larger wall distance presented totally different results.

The last case was a three-dimensional ship. This simulation was also a validation of the 6DOF algorithm but for three dimensions. The ship is studied with linear wave theory and only for heave and pitch motions. The ship is a geosim of a real surface combatant of the US Navy. The STL import function of REEF3D was used for the ship geometry. The level set method definition of the ship geometry was discussed and it enforced the decision of using a grid of dx=0.025 m or finer. Grid dx=0.01 m matched the shape really good however, it would create a huge simulation with the tank geometry so dx=0.025 m was chosen. From the results of the first case, inaccurate results would be expected with the choice of the grid size. However, motions were well described for the grid size, possibly due to the wave theory used and moreover, that surge motion was restrained. Only heave and pitch motion were free. Differences were seen in the troughs for heave motion and the crests for pitch motion.

For all the cases some differences were consistent in the results. In general, the waves generated are correct for both validation cases. Heave motion showed differences in the troughs for both validation cases. Pitch was well described for the two-dimensional simulation. Although, the pitch motion showed differences in the crests for the three-dimensional case. The differences for the three-dimensional ship are not conclusive because of the grid size. Surge motion, for the two-dimensional barge only, had small differences for the negative surge while the positive surge is well represented. With these three cases, the objectives set has been achieved. Heave, pitch and surge comparisons have been performed for two dimensions, and heave and pitch for three dimensions with a good agreement in motions and waves generated. The 6DOF algorithm in REEF3D has been validated for two and three dimensions comparing the numerical results with experimental data proving to work for this kind of problematic. It was also used for two additional cases in two and three dimensions.

4.2 Outlook

The present study has showed that REEF3D can be used for simulations of floating bodies in two and three dimensions. However, more studies are needed in relation to floating bodies. For example, a smaller grid size of the three-dimensional case for validation of the convergence of numerical results. Otherwise, a smaller three-dimensional validation case could be used. Besides, unrestraining more DOF in three dimensions to test them would be desirable, although more EFD data would be needed to confirm, again, the validity of the 6DOF algorithm for the rest of DOF. Additionally, moored structures could be implemented in the software. In the literature, EFD data for validation can be found for moored

structures. Moored structures present several challenges as the motions of the body and the forces on the body are affected because of the additional restrictions of the mooring lines. Also, the forces or the inertia on the mooring lines affects not only the mooring line shape but the body motion. Concluding, REEF3D has a future with work to do in terms of new implementations and functions. Nonetheless, the 6DOF algorithm implemented in REEF3D has been proved to work notably well with free-floating bodies in two and three dimensions.

THIS PAGE INTENTIONALLY LEFT BLANK.

BIBLIOGRAPHY

Ashby, S. F., Falgout, R. D., 1996. A parallel multigrid preconditioned conjugate gradient algorithm for groundwater flow simulations. Nuclear Science and Engineering 124, 145–159.
URL https://www.researchgate.net/publication/239719733_A_parallel_multigrid_preconditioned_conjugate_gradient_algorithm_for_groundwater_flow_simulations

Berthelsen, P. A., Faltinsen, O. M., 2008. A local directional ghost cell approach for incompressible viscous flow problems with irregular boundaries. Journal of Computational Physics 227 (9), 4354–4397.
URL https://www.researchgate.net/publication/238949477_A_local_directional_ghost_cell_approach_for_incompressible_viscous_flow_problems_with_irregular_boundaries

Bihs, H., Kamath, A., Alagan Chella, M., Aggarwal, A., Arntsen, Ø. A., 2016. A new level set numerical wave tank with improved density interpolation for complex wave hydrodynamics. Computers & Fluids 140, 191–208.
URL http://linkinghub.elsevier.com/retrieve/pii/S0045793016302729

Borazjani, I., Ge, L., Sotiropoulos, F., 2008. Curvilinear immersed boundary method for simulating fluid structure interaction with complex 3D rigid bodies. Journal of Computational Physics 227 (16), 7587–7620.
URL https://doi.org/10.1016/j.jcp.2008.04.028

Boussinesq, J., 1877. Essai sur la théorie des eaux courantes.
URL http://gallica.bnf.fr/ark:/12148/bpt6k56673076

Calderer, A., Kang, S., Sotiropoulos, F., 2014. Level set immersed boundary method for coupled simulation of air/water interaction with complex floating structures. Journal of Computational Physics 277, 201–227.
URL http://dx.doi.org/10.1016/j.jcp.2014.08.010

Carrica, P. M., Wilson, R. V., Noack, R. W., Stern, F., 2007. Ship motions using single-phase level set with dynamic overset grids. Computers and Fluids 36 (9), 1415–1433.
URL https://doi.org/10.1016/j.compfluid.2007.01.007

Carrica, P. M., Wilson, R. V., Stern, F., 2006. Unsteady RANS simulation of the ship forward speed diffraction problem. Computers and Fluids 35 (6), 545–570.
URL http://www.sciencedirect.com/science/article/pii/S0045793005000952

Chorin, A., 1968. Numerical Solution of the Navier-Stokes Equations. Mathematics of Computation 22 (104), 745–762.
URL https://doi.org/10.1090/S0025-5718-1968-0242392-2

Courant, R., Friedrichs, K., Lewyt, H., 1967. Courant-Friedrichs-Lewy. IBM Journal (March), 215–234.
URL http://ieeexplore.ieee.org/document/5391985/

Courant, R., Isaacson, E., Rees, M., 1952. On the solution of nonlinear hyperbolic differential equations by finite differences. Communications on Pure and Applied Mathematics 5 (3), 243–255.
URL http://dx.doi.org/10.1002/cpa.3160050303

Dean, R. G., Dalrymple, R. A., 1997. Nonlinear waves. In: Water Wave Mechanics for Engineers and Scientists. World Scientific, Ch. 11, pp. 300–305.
URL http://www.worldscientific.com/worldscibooks/10.1142/1232

Durbin, P. A., 2009. Limiters and wall treatments in applied turbulence modeling. Fluid Dynamics Research 41, 1–18.
URL http://stacks.iop.org/1873-7005/41/i=1/a=012203?key=crossref.efe0f27b27c00dc243b97667392f9b26

Fletcher, R., 1976. Conjugate gradient methods for indefinite systems. Numerical Analysis 506, 73–89.
URL https://www.researchgate.net/publication/239536918_Conjugate_Gradient_Methods_for_Indefinite_Systems

Gaskell, P. H., Lau, A. K. C., 1988. Curvature-compensated convective transport: SMART, A new boundedness preserving transport algorithm. International Journal for Numerical Methods in Fluids 8 (6), 617–641.
URL http://onlinelibrary.wiley.com/doi/10.1002/fld.1650080602/full

Henson, V. E., Yang, U. M., 2002. BoomerAMG: A parallel algebraic multigrid solver and preconditioner. Applied Numerical Mathematics 41 (1), 155–177.
URL https://doi.org/10.1016/S0168-9274(01)00115-5

Hestenes, M., Stiefel, E., 1952. Methods of conjugate gradients for solving linear systems.
URL http://nvlpubs.nist.gov/nistpubs/jres/049/jresv49n6p409_A1b.pdf

Hossain, M., Rodi, W., 1980. Mathematical modelling of vertical mixing in stratified channel flow. In: Proceedings of the 2nd Symposium on Stratified Flows. pp. 280–290.

Irvine, M., Longo, J., Stern, F., 2008. Pitch and Heave Tests and Uncertainty Assessment for a Surface Combatant in Regular Head Waves. Journal of Ship Research 52 (2), 146–163.
URL https://www.researchgate.net/publication/233604308_Pitch_and_Heave_Tests_and_Uncertainty_Assessment_for_a_Surface_Combatant_in_Regular_Head_Waves

Issa, R. I., 1986. Solution of the implicitly discretised fluid flow equations by operator-splitting. Journal of Computational Physics 62 (1), 40–65.
URL https://doi.org/10.1016/0021-9991(86)90099-9

Jiang, G.-S., Shu, C.-W., 1996. Efficient Implementation of Weighted ENO Schemes. Journal of Computational Physics 126 (1), 202–228.
URL http://linkinghub.elsevier.com/retrieve/pii/S0021999196901308

Kamath, A., Alagan Chella, M., Bihs, H., Arntsen, Ø. A., 2015. Evaluating wave forces on groups of three and nine cylinders using a 3D numerical wave tank. Engineering Applications of Computational Fluid Mechanics 9 (1), 343–354.
URL http://www.tandfonline.com/doi/full/10.1080/19942060.2015.1031318

Koo, W., Kim, M. H., 2004. Freely floating-body simulation by a 2D fully nonlinear numerical wave tank. Ocean Engineering 31 (16), 2011–2046.

Krogstad, H. E., Arntsen, Ø. A., 2003. Linear Wave Description and Theory. In: TBA4265 Marine Physical Environment. NTNU, pp. 39–130.
URL http://folk.ntnu.no/oivarn/hercules_ntnu/LWTcourse/lwt_new_2000_Part_A.pdf

Larsen, J., Dancy, H., 1983. Open boundaries in short wave simulations–A new approach. Coastal Engineering 7, 285–297.
URL https://doi.org/10.1016/0378-3839(83)90022-4

Launder, B., Spalding, D., 1974. The numerical computation of turbulent flows. Computer Methods in Applied Mechanics and Engineering 3 (2), 269–289.
URL https://doi.org/10.1016/0045-7825(74)90029-2

Lax, P., Richtmyer, R., 1956. Survey of the Stability of Linear Finite Difference Equations. Communications on pure and applied mathematics IX, 267–293.
URL http://www.mathe.tu-freiberg.de/~ernst/Lehre/IVP/Literatur/laxRichtmyer1956.pdf

Leonard, B. P., 1975. A stable and accurate convective modelling procedure based on quadratic upstream interpolation. Computer Methods in Applied Mechanics and Engineering 19, 59–98.

URL http://dns2.asia.edu.tw/~ysho/YSHO-English/2000%20Engineering/PDF/Com%20Met%20App%20Mec%20Eng19,%2059.pdf

Longo, J., Shao, J., Irvine, M., Stern, F., 2007. Phase-Averaged PIV for the Nominal Wake of a Surface Ship in Regular Head Waves. Journal of Fluids Engineering 129 (5), 524.
URL http://fluidsengineering.asmedigitalcollection.asme.org/article.aspx?articleid=1431204

Naot, D., Rodi, W., 1982. Calculation of secondary currents in channel flow. Journal of the Hydraulics Division 108 (8), 948–968.
URL https://www.researchgate.net/publication/279579615_Calculation_of_secondary_current_in_channel_flow

Ong, M. C., Kamath, A., Bihs, H., Afzal, M. S., 2017. Numerical simulation of free-surface waves past two semi-submerged horizontal circular cylinders in tandem. Marine Structures 52, 1–14.
URL http://dx.doi.org/10.1016/j.marstruc.2016.11.002

Osher, S., Sethian, J. A., 1988. Fronts propagating with curvature-dependent speed: Algorithms based on Hamilton-Jacobi formulations. Journal of Computational Physics 79 (1), 12–49.
URL https://doi.org/10.1016/0021-9991(88)90002-2

Patankar, S. V., Spalding, D. B., 1972. A calculation procedure for heat, mass and momentum transfer in three-dimensional parabolic flows. International Journal of Heat and Mass Transfer 15 (10), 1787–1806.
URL https://doi.org/10.1016/0017-9310(72)90054-3

Peng, D., Merriman, B., Osher, S., Zhao, H., Kang, M., 1999. A PDE-Based Fast Local Level Set Method. Journal of Computational Physics 155 (2), 410–438.
URL http://www.sciencedirect.com/science/article/pii/S0021999199963453

Peskin, C. S., 2002. The immersed boundary method. Acta Numerica 2002, 479–517.
URL https://doi.org/10.1017/S0962492902000077

Ren, B., He, M., Dong, P., Wen, H., 2015. Nonlinear simulations of wave-induced motions of a freely floating body using WCSPH method. Applied Ocean Research 50, 1–12.
URL http://dx.doi.org/10.1016/j.apor.2014.12.003

Schäffer, H. A., Klopman, G., 2000. Review of multidirectional active wave absorption methods. Journal of Waterway, Port, Coastal, and Ocean Engineering 126 (April), 88–97.
URL http://dx.doi.org/10.1061/(ASCE)0733-950X(2000)126:2(88)#sthash.tVKa0RrP.dpuf

Schlichting, H., 1979. Boundary-Layer Theory. McGraw-Hill Book Company.
URL http://link.springer.com/10.1007/978-3-662-52919-5

Shen, Z., Wan, D., 2013. RANS computations of added resistance and motions of a ship in head waves. International Journal of Offshore and Polar Engineering 23 (4), 263–271.
URL https://www.onepetro.org/journal-paper/ISOPE-13-23-4-263

Shu, C. W. and Osher, S., 1988. Efficient implementation of essentially non-oscillatory shock capturing schemes. Journal of Computational Physics 77, 439–471.
URL https://doi.org/10.1016/0021-9991(88)90177-5

Smagorinsky, J., 1963. General Circulation Experiments With the Primitive Equations. Monthly Weather Review 91 (3), 99–164.
URL https://docs.lib.noaa.gov/rescue/mwr/091/mwr-091-03-0099.pdf

Stokes, G. G., 1847. On the Theory of Oscillatory Waves. Cambridge Philosophical Society 8, 197–237.
URL http://pordlabs.ucsd.edu/wryoung/theorySeminar/pdf15/Stokes1847.pdf

Stone, H. L., 1968. Multidimensional Partial Differential Equations. SIAM Journal on Numerical Analysis 5 (3), 530–558.
URL http://epubs.siam.org/doi/abs/10.1137/0705044

Takashi, N., 1994. ALE finite element computations of fluid-structure interaction problems. Computer Methods in Applied Mechanics and Engineering 112 (1-4), 291–308.
URL https://doi.org/10.1016/0045-7825(94)90031-0

Tanaka, S., Kashiyama, K., 2006. ALE finite element method for FSI problems with free surface using mesh re-generation method based on background mesh. International Journal Of Computational Fluid Dynamics 20 (3-4), 229–236.
URL http://dx.doi.org/10.1080/10618560600811471

van der Vorst, H., 1992. Bi-CGSTAB: a fast and smoothly converging variant of bi-CG for the solution of nonsymmetric linear systems. SIAM Journal on Scientific and Statistical Computing 13 (2), 631–644.
URL http://epubs.siam.org/doi/abs/10.1137/0913035

Versteeg, H. K., Malalasekera, W., 2007. An Introduction to Computational Fluid Dynamics. Vol. 1. Pearson.
URL https://www.pearsonhighered.com/program/Versteeg-An-Introduction-to-Computational-Fluid-Dynamics-The-Finite-Volume-Method-2nd-Edition/PGM299497.html

Wallin, S., Johansson, A. V., 2000. An explicit algebraic Reynolds stress model for incompressible and compressible turbulent flows. Journal of Fluid Mechanics 403, 89–132.
URL https://doi.org/10.1017/S0022112099007004

Wilcox, D. C., 1995. Turbulence Modelling for CFD. Journal of Fluid Mechanics 289, 406–407.
URL https://doi.org/10.1017/S0022112095211388

Yang, J., Stern, F., 2009. Sharp interface immersed-boundary/level-set method for wave-body interactions. Journal of Computational Physics 228 (17), 6590–6616.
URL http://dx.doi.org/10.1016/j.jcp.2009.05.047

Yoon, H., 2009. Phase-averaged stereo-PIV flow field and force / moment / motion measurements for surface combatant in PMM maneuvers. Ph.D. thesis, University of Iowa.
URL http://ir.uiowa.edu/cgi/viewcontent.cgi?article=1638&context=etd

Zhiyin, Y., 2015. Large-eddy simulation: Past, present and the future. Chinese Journal of Aeronautics 28 (1), 11–24.
URL http://dx.doi.org/10.1016/j.cja.2014.12.007